



| | |
|----------------------------------|--|
| Publication Year | 2019 |
| Acceptance in OA | 2022-02-24T13:42:18Z |
| Title | The SOMA Radio Survey. I. Comprehensive SEDs of High-mass Protostars from Infrared to Radio and the Emergence of Ionization Feedback |
| Authors | Rosero, V., Tanaka, K. E. I., Tan, J. C., Marvil, J., Liu, M., Zhang, Y., De Buizer, J. M., BELTRAN SOROLLA, MARIA TERESA |
| Publisher's version (DOI) | 10.3847/1538-4357/ab0209 |
| Handle | http://hdl.handle.net/20.500.12386/31460 |
| Journal | THE ASTROPHYSICAL JOURNAL |
| Volume | 873 |

THE SOMA RADIO SURVEY. I. COMPREHENSIVE SEDS OF HIGH-MASS PROTOSTARS FROM INFRARED TO RADIO AND THE EMERGENCE OF IONIZATION FEEDBACK

V. ROSERO^{1,2,3}, K. E. I. TANAKA^{4,5,3}, J. C. TAN^{6,2}, J. MARVIL¹, M. LIU^{2,3}, Y. ZHANG⁷, J. M. DE BUIZER⁸, M. T. BELTRÁN⁹

¹National Radio Astronomy Observatory, 1003 Lopezville Rd., Socorro, NM 87801, USA

²Department of Astronomy, University of Virginia, Charlottesville, VA 22904, USA

³Department of Astronomy, University of Florida, Gainesville, FL 32611, USA

⁴Department of Earth and Space Science, Osaka University, Toyonaka, Osaka 560-0043, Japan

⁵Chile Observatory, National Astronomical Observatory of Japan, Mitaka, Tokyo 181-8588, Japan

⁶Dept. of Space, Earth and Environment, Chalmers University, SE-412 96 Gothenburg, Sweden

⁷Star and Planet Formation Laboratory, RIKEN Cluster for Pioneering Research, Wako, Saitama 351-0198, Japan

⁸SOFIA-USRA, NASA Ames Research Center, MS 232-12, Moffett Field, CA 94035, USA

⁹INAF, Osservatorio Astrofisico di Arcetri, Largo E. Fermi 5, 50125 Firenze, Italy

ABSTRACT

We study centimeter continuum emission of eight high- and intermediate-mass protostars that are part of the *SOFIA* Massive (SOMA) Star Formation Survey, thus building extended spectral energy distributions (SEDs) from the radio to the infrared. We discuss the morphology seen in the centimeter continuum images, which are mostly derived from archival VLA data, and the relation to infrared morphology. We use the SEDs to test new models of high-mass star formation including radiative and disk-wind feedback and associated free-free and dust continuum emission (Tanaka, Tan, & Zhang 2016). We show that interferometric data of the centimeter continuum flux densities provide additional, stringent tests of the models by constraining the ionizing luminosity of the source and help to break degeneracies encountered when modeling the infrared-only SEDs, especially for the protostellar mass. Our derived parameters are consistent with physical parameters estimated by other methods such as dynamical protostellar masses. We find a few examples of additional stellar sources in the vicinity of the high-mass protostars, which may be low-mass young stellar objects. However, the stellar multiplicity of the regions, at least as traced by radio continuum emission, appears to be relatively low.

Keywords: ISM: jets and outflows – stars: formation – techniques: interferometric

1. INTRODUCTION

High-mass stars ($m_* \geq 8M_\odot$) are important throughout astrophysics, but their mechanism of formation is still actively debated (see, e.g., Tan et al. 2014 for a review). For traditional star formation models based on Core Accretion, there is a proposed evolutionary sequence as the protostar grows in mass. For example, based on the Turbulent Core Accretion model (McKee & Tan 2003), Zhang, Tan, & Hosokawa (2014) and Zhang & Tan (2018) have presented a sequence of protostellar evolution and infrared continuum radiative transfer models exclusively developed for intermediate and high-mass stars. These can be compared to observed infrared and sub-mm spectral energy distributions (SEDs) and images to constrain the properties of the protostar (e.g., Zhang et al. 2013; De Buizer et al. 2017).

High-mass protostars are generally expected to become fairly bright centimeter continuum sources (flux densities of \sim few mJy to Jy), as the stellar photosphere heats up and begins to ionize its surroundings. Centimeter continuum observations, especially with the improved capabilities of the Karl G. Jansky Very Large Array (VLA)¹, are therefore able to provide unique insights into the earliest, embedded phases of high-mass star birth. Moreover, Tanaka, Tan, & Zhang (2016, hereafter TTZ16) calculated the predicted ionization structures and centimeter continuum emission properties using the initial parameters resulting from the radiative transfer models. In this framework, the earliest stages of ionizing feedback involve the ionization of a magnetohydrodynamical driven disk wind and/or X-wind, which would appear as a thermal radio jet (see also Tan & McKee 2003). Later, once the outflow is fully ionized, the ionizing photons begin to interact with the infall envelope and disk, potentially driving a

¹The National Radio Astronomy Observatory is a facility of the National Science Foundation operated under cooperative agreement by Associated Universities, Inc.

photoevaporative outflow. Alternative models have been discussed in the literature, including those involving ionized accretion flows at the center of the core (Keto 2007). More radically, alternative formation scenarios invoking competitive accretion (Bonnell et al. 2001; Wang et al. 2010) or even protostellar collisions (Bonnell et al. 1998; Bally & Zinnecker 2005) are expected to involve much more disordered accretion flows to the protostar (see also Dale et al. 2005) and these may become illuminated by their radio emission once the protostars start ionizing their surroundings.

High-mass star-forming regions are composed of one or more cores or dense substructures occupying $\lesssim 0.1$ pc scales. When there are multiple sources present, these may be in different evolutionary stages, from prestellar to protostellar. The latter begin to show greater astrochemical complexity as the protostar warms up the inner region, appearing as hot molecular cores (HMCs). Rosero et al. (2016), using the VLA and achieving image rms noise values of $\sim 3\text{--}10$ $\mu\text{Jy}/\text{beam}$, found that HMCs are very commonly associated with centimeter wavelength sources, most of them with low radio emission levels on the order of < 1 mJy. Moreover, many of these centimeter continuum sources have morphologies and parameters that resemble ionized jets, which is in general agreement with results from the TTZ16 modeling. Thus, radio continuum emission is extremely relevant in order to constrain the ionizing luminosity of the protostar.

Physical parameters such as the mass of the hosting core, the mass of the central protostar and the mass accretion rate are extremely important to characterize the evolution of forming high-mass stars, but obtaining accurate estimates of these parameters is rather challenging. Thus, the testing and calibration of new theoretical models which predict such parameters using observational data are urgently needed. Our overall goal now is to assemble multi-wavelength data for a statistically significant sample of high- and intermediate-mass protostars and use the data to test theoretical models of their formation and feedback mechanisms. Our sample will probe different environments, evolutionary stages and core masses using observations from the MIR, FIR, sub-mm/mm and centimeter wavelengths. The *SOFIA* Massive (SOMA) Star Formation Survey (PI: Tan) aims to observe ~ 50 high- and intermediate-mass protostars with *SOFIA*-FORCAST at $\sim 10\text{--}40$ μm . Such data, together with ancillary *Herschel* data, help define the peak of the SED, thus constraining the bolometric luminosity of the protostars. Furthermore the $\sim 10\text{--}40$ μm images trace warm dust delineating protostellar outflow cavities, which helps determine the geometry of the protostellar source. Extinction of this cavity emission by the colder, dense core envelope also constrains properties of the protostellar core. The SOMA survey sample consists of a range of four source types that have been defined in De Buizer et al. (2017) (i.e., Type I to Type IV), from isolated MIR sources within otherwise infrared dark clouds (IRDCs) lacking centimeter continuum emission (i.e., Type I) at an image rms level ~ 0.3 mJy/beam (typical of the CORNISH survey; Purcell et al. 2008), to more evolved sources with known centimeter continuum emission of various extents (i.e., Type II and Type III for association with hypercompact(HC) or ultracompact(UC) HII regions, respectively), to clustered (within $\sim 60''$) MIR sources that are sometimes known to be associated with radio emission (i.e., Type IV). So far, 22 sources from the SOMA survey have been observed with *SOFIA*-FORCAST and results for the first eight protostars from the sample are presented in De Buizer et al. (2017, hereafter DLT17). These results include the derivation of SEDs and then model fitting using the theoretical Zhang & Tan (2018, hereafter ZT18) models developed exclusively for high- and intermediate-mass protostars. In particular, the protostellar mass, accretion rate and core envelope mass are estimated. The geometries of the cores are also constrained: e.g., the near-facing, blue-shifted side of the outflow has a cavity that typically appears brighter at shorter IR wavelengths compared to the far-facing, redshifted side. However, there are still significant degeneracies in parameters derived from infrared SEDs alone, such as the protostellar masses and bolometric luminosities that even for the best models have relatively large allowed ranges. Our goal with this study is to use the centimeter emission data and the associated predictions of centimeter continuum free-free emission from TTZ16 to help break these degeneracies.

Previous observational studies such as the Red MSX Source (RMS) survey (e.g., Hoare et al. 2005; Mottram et al. 2007; Urquhart et al. 2009) have made progress towards multi-wavelength observations and studies of high-mass protostars located throughout the Galaxy. Their observations are mainly based upon the Midcourse Space Experiment (MSX) survey (Price et al. 2001) and Two Micron All Sky Survey (2MASS) data for the infrared as well as centimeter continuum from the VLA at 6 cm with spatial resolutions of $\sim 1\text{--}2''$ and image rms noise of ~ 0.22 mJy. However, our FORCAST data has $\sim 6\times$ higher resolution than the MSX survey at $\sim 20\mu\text{m}$, and we are often resolving multiple sources of emission that appear as single sources in MSX, allowing for more precise photometry. Also, with the FORCAST data we have extended the wavelength coverage of the SEDs beyond the longest filter of MSX, which was $21.3\mu\text{m}$. Furthermore, the FORCAST filters have narrower bandpasses, and are therefore more accurate at estimating the flux at a given wavelength.

Previous relevant theoretical studies have included numerical simulations of massive star formation that incorporate MHD outflow feedback (e.g., Cunningham et al. 2011; Kuiper et al. 2016; Matsushita et al. 2017; Staff et al. 2018; Kuiper & Hosokawa 2018; Kölligan & Kuiper 2018). However, in general the outputs of these simulations have not been coupled to detailed radiative transfer calculations for both the thermal dust and radio continuum (free-free) emission from ionized gas. Nor do these models span a wide range of environmental conditions. Thus our approach in this paper is to use the observational data to test simpler semi-analytic models, i.e., the ZT18 grid of models for thermal dust emission from massive protostars and the TTZ16 models for

radio continuum emission from ionized gas calculated self-consistently from the ZT18 physical models.

In this paper, we present extended SEDs to include centimeter continuum fluxes for the eight regions studied by [DLT17](#) and which are under the SOMA Type II category, specifically because the MIR emission extends beyond the observed radio emission. All these sources are known to be associated with large scale molecular outflows except for IRAS 07299–1651 due to its limited observational data. We primarily used high-sensitivity Jansky VLA public archival data at 6, 1.3 and 0.7 cm to determine the flux densities of the regions in order to test the [TTZ16](#) model. We used information from the literature when the regions did not have any public Jansky VLA data available. In order to investigate the morphology and the multiplicity of the radio sources associated to our eight SOMA regions, we focused on available high angular resolution data; in most cases the data presented in this paper at the shorter wavelengths are $\sim 10\times$ higher resolution than at larger wavelengths. The methodology and public archival data are presented in §2. A description of the [TTZ16](#) models is in §3. Basic observational results are presented in §4, while analysis and testing of the [TTZ16](#) models are in §5. The discussion and summary are presented in §6 and §7, respectively.

2. METHODS

The SOMA Star Formation Survey sample is defined by *SOFIA*-FORCAST observations (i.e., from ~ 10 to $40 \mu\text{m}$), with the first eight sources presented by [DLT17](#). These eight sources define the sample for which we present and analyze the radio data in this paper. The radio observations presented here are mostly public Jansky VLA data retrieved from the VLA data archive, except for regions G45.47+0.05 (at 6 cm) and Cepheus A where we used information available in the literature and region IRAS 07299–1651 where we present our own observations.

The archival and literature data that we analyzed in this work are summarized in Table 1. Column 1 gives the region name, and column 2, 3 and 4 give the band frequency, R.A., and declination, while columns 5 and 6 give the synthesized beam size and position angle (PA) and the rms of the resulting images. The distance to every region, as adopted by [DLT17](#), as well as the bolometric luminosities evaluated by [DLT17](#), are shown in columns 7 and 8, respectively.

The references for the radio fluxes that were obtained from the literature are in column 9. A list of phase calibrators used in the observations at 6, 1.3 and 0.7 cm is given in Table 2.

Table 1. SOMA Sources: Radio Continuum Data

| Region | Frequency Band (GHz) | R.A. (J2000) | Dec. (J2000) | Beam Size ("×", deg) | rms ($\mu\text{Jy beam}^{-1}$) | D ^a (kpc) | L ^b ($10^4 L_{\odot}$) | Ref. ^c |
|-----------------|-------------------------|-----------------|-----------------|-------------------------|-------------------------------------|-------------------------|--|-------------------|
| AFGL 4029 | 4.0–8.0 | 03 01 31.28 | +60 29 12.9 | 0.35×0.28, –43.7 | 7.0 | 2.0 | 1.6–34.0 | ... |
| | 40.0–50.0 | ... | ... | 0.06×0.04, +69.7 | 60.0 | ... | ... | ... |
| AFGL 437 | 4.0–8.0 | 03 07 24.55 | +58 30 52.8 | 0.44×0.33, –76.0 | 7.0 | 2.0 | 1.7–15.0 | ... |
| | 40.0–50.0 | ... | ... | 0.06×0.04, +71.7 | 60.0 | ... | ... | ... |
| IRAS 07299–1651 | 4.0–8.0 | 07 32 09.74 | –16 58 11.3 | 0.47×0.29, –9.84 | 7.0 | 1.68 | 1.0–4.2 | ... |
| | ... | ... | ... | ... | ... | ... | ... | ... |
| G35.20–0.74 | 4.0–8.0 | 18 58 13.02 | +01 40 36.2 | 0.54×0.28, –48.5 | 8.0 | 2.2 | 3.8–8.4 | ... |
| | 18.0–26.5 | ... | ... | 0.30×0.25, –12.8 | 18.0 | ... | ... | ... |
| | 40.0–50.0 | ... | ... | 0.17×0.13, –29.1 | 15.0 | ... | ... | ... |
| G45.47+0.05 | 6 cm ^d | 19 14 25.67 | +11 09 25.4 | 1.75×1.57, –78.9 | 1000.0 | 8.4 | 17.0–51.0 | (1) |
| | 40.0–50.0 | ... | ... | 0.05×0.04, –24.2 | 90.0 | ... | ... | ... |
| IRAS 20126+4104 | 4.0–8.0 | 20 14 26.05 | +41 13 32.5 | 0.33×0.29, +65.2 | 6.0 | 1.64 | 2.0–9.3 | (2) |
| | 18.0–26.5 | ... | ... | 0.35×0.24, –85.1 | 10.0 | ... | ... | ... |
| Cepheus A | 3.6 cm ^d | 22 56 17.98 | +62 01 49.4 | 0.27×0.19, –79.1 | 50.0 | 0.7 | 2.4–9.9 | (3) |
| | 1.3 cm ^d | ... | ... | 0.09×0.07, +32.8 | 50.0 | ... | ... | ... |
| | 0.7 cm ^d | ... | ... | 0.05×0.04, –57.9 | 250.0 | ... | ... | ... |

Table 1 continued on next page

Table 1 (*continued*)

| Region | Frequency Band (GHz) | R.A. (J2000) | Dec. (J2000) | Beam Size ("×", deg) | rms (μ Jy beam ⁻¹) | D ^a (kpc) | L ^b (10 ⁴ L _⊙) | Ref. ^c |
|---------------|-------------------------|-----------------|-----------------|-------------------------|--|-------------------------|---|-------------------|
| NGC 7538 IRS9 | 4.0–8.0 | 23 14 01.77 | +61 27 19.8 | 0.32×0.26, +20.7 | 30.0 | 2.65 | 3.7–8.2 | ... |
| | 40.0–50.0 | ... | ... | 0.05×0.04, –5.29 | 43.0 | ... | ... | ... |

^a References cited in [De Buizer et al. \(2017\)](#).

^b Range of bolometric luminosities from the best models reported in [De Buizer et al. \(2017\)](#).

^c References for the literature data.

^d Value from the literature. Data observed using the VLA before the upgrade.

NOTE—The centimeter continuum information of sources G45.47+0.05 (at 6 cm) and Cepheus A were taken from the literature and the references are given in column 9. Also, for the analysis of IRAS 20126+4104, we use the radio images presented in [Rosero et al. \(2016\)](#). Units of right ascension are hours, minutes, and seconds, and units of declination are degrees, arcminutes, and arcseconds.

(1) [Urquhart et al. \(2009\)](#); (2) [Rosero et al. \(2016\)](#); (3) [Curiel et al. \(2006\)](#)

Table 2. VLA Calibrators

| Calibrator | Astrometry Precision ^a | Source Calibrated | Band |
|------------|-----------------------------------|-------------------|---------|
| J0228+6721 | A | AFGL 4029 | C, K, Q |
| J0359+5057 | B | AFGL 437 | C, K |
| J2230+6946 | A | NGC 7538 IRS9 | C, K |
| J0735–1735 | A | IRAS 07299–1651 | C |
| J1851+0035 | C | G35.20–0.74 | C, K |
| J0228+6721 | A | AFGL 437 | Q |
| J1924+1540 | A | G45.47+0.05 | Q |
| J2250+5550 | A | NGC 7538 IRS9 | Q |

^a Astrometric precision A, B, and C correspond to positional accuracies of <2 mas, 2–10 mas, and 0.01–0.15 arcsecs, respectively.

2.1. VLA data

2.1.1. 6 cm Data

The 6 cm (C-band) observations were made in the A configuration providing angular resolutions $\sim 0''.3 - 0''.5$. The data for sources AFGL 4029, AFGL 437 and NGC 7538 IRS9 are from project code 12B–140 from observations taken in 2012 and the data for source G35.20–0.74 are from project code 13B–210 from observations taken in 2013. The data consist of two 1 GHz wide basebands (8 bit samplers) centered at 5.3 and 6.3 GHz, where each baseband was divided into 8 spectral windows (SPWs), each with a bandwidth of 128 MHz. The data were recorded in 16 unique SPWs, each comprised of 64 channels and each channel being 2 MHz wide, resulting in a total bandwidth of 2048 MHz (before “flagging”). 3C48 was used as flux density and bandpass calibrator for regions AFGL 4029 and AFGL 437, and 3C286 was used as flux density and bandpass calibrator for regions G35.20–0.74 and NGC 7538 IRS9. For sources AFGL 4029, AFGL 437 and NGC 7538 IRS9 the observations were made alternating on a target source for ~ 13 minutes and a phase calibrator for ~ 1 minute, for a total on-source time of ~ 26 minutes. For G35.20–0.74 the observations were made alternating on a target source for ~ 10 minutes and a phase calibrator for ~ 1 minute, for a total on-source time of ~ 40 minutes.

The observations for source IRAS 07299–1651 are from project code 18A–294 (PI: Rosero) taken in 2018 and the data consists of two ~ 2 GHz wide basebands (3 bit samplers) centered at 5.03 and 6.98 GHz. The data were recorded in 30 unique SPWs, each comprised of 64 channels and each channel being 2 MHz wide, resulting in a total bandwidth of 3842 MHz (before “flagging”).

3C48 was used as flux density and bandpass calibrator and the observations were made alternating on a target source for ~ 9.5 minutes and a phase calibrator for ~ 40 seconds, for a total on-source time of ~ 37 minutes.

The data were processed using NRAO’s Common Astronomy Software Applications (CASA)² package. Eight channels at the edges of each baseband were flagged due to substantial band roll-off (and therefore loss of sensitivity). In addition, we inspected the data for radio frequency interference (RFI) or other problems, performing “flagging” when needed. The flux density scale was set via standard NRAO models using the task `setjy` for the flux calibrators and using the [Perley & Butler \(2013\)](#) flux scale. We used the `gencal` task to check for antenna position corrections and also to apply gain curve and antenna efficiency factors. Delay and bandpass solutions were formed based on observations of the flux density calibrator. These solutions were applied when solving for the final amplitude and phase calibration using the task `gaincal` over the full bandwidth. We measured the flux density of the phase calibrators using the task `fluxscale`. The amplitude, phase, delay and bandpass solutions were applied to the target sources using the task `applycal`. The images were made using the `tclean` task and Briggs `Robust=0.5` weighting. For source G35.20–0.74 we performed self-calibration.

For regions AFGL 4029, AFGL 437, G35.20–0.74 and NGC 7538 IRS9, we made two images, each of ~ 1 GHz baseband composed of 8 SPWs and also a combined image using data from both basebands with a total of 16 SPWs. For region IRAS 07299–1651 we made two images, each of ~ 2 GHz baseband composed of 15 SPWs and also a combined image using data from both basebands with a total of 30 SPWs. All maps were primary-beam-corrected. Table 1 columns 5 and 6 show the synthesized beam (size and position angle) and the rms of the combined images.

2.1.2. 1.3 cm Data

The 1.3 cm (*K*-band) observations were made in the B configuration providing angular resolutions $0''.3$. The data reduced in this work is for source G35.20–0.74 (project code 13B–033) from observations taken in 2013. The data consists of two 4 GHz wide basebands (3 bit samplers) centered at 19.9 and 23.9 GHz, where each baseband was divided into 32 spectral windows (SPWs), each with a bandwidth of 128 MHz. The data were recorded in 64 unique SPWs, each comprised of 128 channels and each channel being 1 MHz wide, resulting in a total bandwidth of 8192 MHz (before “flagging”). 3C286 was used as the flux density and bandpass calibrator for region G35.20–0.74. The observations were made alternating on a target source for ~ 2.5 minutes and a phase calibrator for ~ 1 minute, for a total on-source time of ~ 7 minutes.

The data reduction was done in the same fashion as that for the 6 cm observations. In addition, we corrected for atmospheric opacity using the weather station information from the `plotWeather` task and creating the calibration table using `gencal`. The images were made using the `tclean` task and Briggs `Robust=0.5` weighting. We made two images, each of ~ 4 GHz baseband composed of 32 SPWs and also a combined image using data from both basebands with a total of 64 SPWs. All maps were primary-beam-corrected. Table 1 columns 5 and 6 show the synthesized beam (size and position angle) and the rms of the combined images.

2.1.3. 0.7 cm Data

The 0.7 cm (*Q*-band) observations were made in the A configuration — except for G35.20–0.74 where B configuration was used — providing angular resolutions $\sim 0''.04 - 0''.06$ and $\sim 0''.2$ for the B configuration data. The data for sources AFGL 4029 and AFGL 437 are from project code 15A–238 from observations taken in 2015, the data for source G35.20–0.74 is from project code 13B–210 from observations taken in 2013, the data for source G45.47+0.05 is from project code 14A–113 from observations taken in 2014, and the data for source NGC 7538 IRS9 is from project code 14A–092 from observations taken in 2014. The data for sources AFGL 4029, AFGL 437 and NGC 7538 IRS9 consist of two 4 GHz wide basebands (3 bit samplers) centered at 41.9 and 45.9 GHz, where each baseband was divided into 32 spectral windows (SPWs), each with a bandwidth of 128 MHz. The data were recorded in 64 unique SPWs, each comprised of 64 channels and each channel being 2 MHz wide, resulting in a total bandwidth of 8192 MHz (before “flagging”). The correlator setup for the observations of sources G35.20–0.74 and G45.47+0.05 was the same as that used at 1.3 cm, with the two basebands centered at 41.9 and 45.9 GHz. 3C48 was used as flux density and bandpass calibrators for regions AFGL 4029, AFGL 437 and NGC 7538 IRS9, and 3C286 were used as flux density and bandpass calibrators for regions G35.20–0.74 and G45.47+0.05. For sources AFGL 4029 and AFGL 437 the observations were made alternating on a target source for ~ 1.7 minutes and a phase calibrator for ~ 1 minute, for a total on-source time of ~ 7 minutes. For G35.20–0.74 the observations were made alternating on a target source for ~ 2.5 minutes and a phase calibrator for ~ 1 minute, for a total on-source time of ~ 38 minutes. For G45.47+0.05 the observations were made alternating on a target source for ~ 2 minutes and a phase calibrator for ~ 1 minute, for a total on-source time of ~ 23 minutes. For NGC 7538 IRS9 the observations were made alternating on a target source for ~ 2 minutes and a phase calibrator for ~ 1 minute, for a total on-source time of ~ 11 minutes.

² <http://casa.nrao.edu>

The data reduction was done in the same fashion as that for the 6 cm observations. In addition, we corrected for atmospheric opacity using the weather station information from the `plotWeather` task and creating the calibration table using `gencal`. The images were made using the `tclean` task and Briggs Robust=0.5 weighting. For source G45.47+0.054 we performed self-calibration. We made two images, each of ~ 4 GHz baseband composed of 32 SPWs and also a combined image using data from both basebands with a total of 64 SPWs. All maps were primary-beam-corrected. Table 1 columns 5 and 6 show the synthesized beam (size and position angle) and the rms of the combined images.

3. THEORETICAL MODELS

[DLT17](#) investigated the protostellar properties of the eight SOMA sources presented in this paper, fitting the given set of infrared observations to the ZT model grid. However, the obtained properties of the IR-only SED models still have relatively large allowed variations in their parameters, i.e., significant degeneracies. In this paper, we aim to constrain the models further by comparing the radio observations and the [TTZ16](#) model of free-free emission. In this section, we briefly revisit these theoretical models, i.e., the ZT and [TTZ16](#) models, and the model selection methods.

3.1. ZT model grid for dust thermal emission

In high-mass star formation, the vast majority of the energy emitted from the protostar and the innermost accretion flow is at optical and UV wavelengths. However, it is hard to directly detect the radiation from the protostar and its vicinity because most of the flux emitted at those wavelengths is immediately absorbed by the surrounding material and reemitted in the infrared. Therefore, in order to investigate the properties of the embedded protostar, theoretical synthetic observational modeling is necessary. In a series of papers ([Zhang & Tan 2011](#); [Zhang et al. 2013, 2014](#); [Zhang & Tan 2018](#)) a theoretical model of the evolution of high-mass protostars based on the Turbulent Core scenario ([McKee & Tan 2003](#)) has been developed, which provides the continuum flux at infrared and optical wavelengths. These are referred to as the ZT models.

In the ZT models, massive protostars are assumed to form from massive prestellar cores. The prestellar core properties are parameterized by the initial core mass M_c and the mass surface density of the ambient clump Σ_{cl} . The latter determines the surface pressure of cores, and thus sets their sizes and densities together with M_c . The core undergoes collapse that forms a protostar-disk system at its center. The infalling structure is given by the self-similar solution ([McLaughlin & Pudritz 1997](#)) including effects of rotation ([Ulrich 1976](#)). The disk structure is described with an α -disk solution ([Shakura & Sunyaev 1973](#)), with an improved treatment including the infall to and outflow from the disk. The accretion rate onto the protostar is regulated by the feedback of the MHD disk wind ([Blandford & Payne 1982](#); [Matzner & McKee 2000](#)). The protostellar evolution is calculated consistently to the accretion rate based on the method developed by [Hosokawa & Omukai \(2009\)](#) and [Hosokawa et al. \(2010\)](#), solving the basic stellar structure equations, i.e., continuity, hydrostatic balance, energy conservation and transfer.

The evolution of the protostar and its surrounding gas structure are calculated self-consistently from the initial core parameters, i.e., M_c and Σ_{cl} . The protostellar mass m_* is used as the third parameter to specify a particular stage of the evolutionary tracks. The continuum radiative transfer calculations at infrared and optical wavelengths have been performed for 432 physical models defined by different sets of (M_c, Σ_{cl}, m_*) using the latest version of the Monte Carlo code, HOCHUNK3d ([Whitney et al. 2003, 2013](#)). For each model, 20 inclination angles θ_{view} are sampled evenly in cosine space to produce the SEDs. To compare with the observations, a variable foreground extinction A_V is applied to the model SEDs. Thus, for a given source distance, a set of five parameters of $(M_c, \Sigma_{cl}, m_*, \theta_{view}, A_V)$ gives one SED in the ZT model grid.

In [DLT17](#), the authors searched for the best fit models for the eight SOMA regions presented in this paper from the ZT model grid to investigate the properties of their protostars and surrounding gas. They used χ^2 minimization (in log space) to find the best models to fit a given set of observations at 8–70 μm for the eight SOMA sources. They successfully found models that can explain the infrared observed SED of each of these SOMA sources. However, even among the best five models, the obtained protostellar properties, such as stellar masses and bolometric luminosities, have relatively large degeneracies.

3.2. TTZ16 model for free-free emission

To further constrain the protostellar properties we use the additional diagnostic of free-free emission from photoionized gas. The UV flux dramatically increases during the Kelvin-Helmholtz (KH) contraction phase in the formation of a high-mass star, although this cannot be directly observed due to absorption by the surrounding gas and dust. However, the gas absorbing Lyman continuum photons with > 13.6 eV becomes ionized and emits thermal bremsstrahlung, i.e., free-free emission. Therefore, free-free emission at radio wavelengths from the photoionized region can provide the direct signpost of the evolutionary state of the embedded protostar.

Using the physical parameters of the best five models for the infrared, we calculated the photoionized structures and the free-free flux from them using the method of [TTZ16](#). The basic protostellar properties and the density structure of the surrounding material are given from the ZT model grids. The ionizing photon rate is evaluated using the stellar atmosphere model of [Castelli](#)

& Kurucz (2004). The temperature of the ionized gas is evaluated by CLOUDY (Ferland et al. 2013). The photoionized structure is obtained by the ray-tracing radiative transfer calculation (Stone et al. 1992; Tanaka et al. 2013), which allows a treatment of both the direct and diffuse ionizing radiation fields.

Some hydrodynamical simulations have included the MHD outflow feedback in high-mass star formation (e.g., Kuiper et al. 2016; Matsushita et al. 2017). Especially, Kuiper & Hosokawa (2018) recently performed the first simulations self-consistently including the protostellar outflow together with the radiation force and the photoionization feedback. However, since they focused on the dynamical impact of feedback processes, they have not conducted the observational modeling for dust and free-free emissions. Moreover, they explored only two initial conditions, while our semi-analytic models span a wide range of environmental conditions (TTZ16; Tanaka et al. 2017). We note that the predictions of our semi-analytic models, such as the star formation efficiencies, are quantitatively consistent with those from simulations by Kuiper & Hosokawa (2018), which supports the accuracy of our semi-analytic models.

Table 3. AFGL 4029: Parameters from Radio Continuum

| Scale | R.A. (J2000) | Dec. (J2000) | S _{5.3 GHz} (mJy) | S _{6.3 GHz} (mJy) | S _{41.9 GHz} (mJy) | S _{45.9 GHz} (mJy) | Spectral Index |
|--------------|-----------------|-----------------|-------------------------------|-------------------------------|--------------------------------|--------------------------------|-------------------|
| SOMA | 03:01:31.28 | +60:29:12.9 | 0.44(0.52) | 0.42(0.77) | 4.73(30.04) | <134.24 | <1.1 |
| Intermediate | 03:01:31.28 | +60:29:12.9 | 0.31(0.06) | 0.34(0.08) | 0.95(3.12) | <14.10 | <0.5 |
| Inner | 03:01:31.28 | +60:29:12.8 | 0.14(0.02) | 0.16(0.03) | 0.74(0.11) | 0.48(0.11) | 0.7(0.1) |

NOTE—The intermediate scale corresponds to the extent of the radio jet. Units of right ascension are hours, minutes, and seconds, and units of declination are degrees, arcminutes, and arcseconds.

Table 4. AFGL 437: Parameters from Radio Continuum

| Scale | R.A. (J2000) | Dec. (J2000) | S _{5.3 GHz} (mJy) | S _{6.3 GHz} (mJy) | S _{41.9 GHz} (mJy) | S _{45.9 GHz} (mJy) | Spectral Index |
|--------------|-----------------|-----------------|-------------------------------|-------------------------------|--------------------------------|--------------------------------|-------------------|
| SOMA | 03:07:24.49 | +58:30:42.8 | 0.82(0.28) | 0.36(0.57) | 0.28(10.34) | 3.37(15.54) | -4.7(3.6) |
| Intermediate | ... | ... | ... | ... | ... | ... | ... |
| Inner | 03:07:24.49 | +58:30:42.8 | 0.77(0.09) | 0.80(0.09) | 1.39(0.20) | 1.57(0.30) | 0.3(0.1) |

NOTE—Units of right ascension are hours, minutes, and seconds, and units of declination are degrees, arcminutes, and arcseconds.

Table 5. IRAS 07299–1651: Parameters from Radio Continuum

| Scale | R.A. (J2000) | Dec. (J2000) | S _{5.0 GHz} (mJy) | S _{7.0 GHz} (mJy) | Spectral Index |
|--------------|-----------------|-----------------|-------------------------------|-------------------------------|-------------------|
| SOMA | 07:32:09.74 | -16:58:11.3 | 1.56(0.25) | 1.62(0.34) | 0.1(0.8) |
| Intermediate | ... | ... | ... | ... | ... |
| Inner | 07:32:09.79 | -16:58:10.9 | 1.15(0.12) | 1.47(0.16) | 0.7(0.5) |

NOTE—Units of right ascension are hours, minutes, and seconds, and units of declination are degrees, arcminutes, and arcseconds.

Table 6. G35.20-0.74: Parameters from Radio Continuum

| Scale | R.A. (J2000) | Dec. (J2000) | S _{4.9 GHz} (mJy) | S _{6.9 GHz} (mJy) | S _{19.9 GHz} (mJy) | S _{23.9 GHz} (mJy) | S _{41.9 GHz} (mJy) | S _{45.9 GHz} (mJy) | Spectral Index |
|--------------|-----------------|-----------------|-------------------------------|-------------------------------|--------------------------------|--------------------------------|--------------------------------|--------------------------------|-------------------|
| SOMA | 18:58:13.02 | +01:40:36.2 | 15.08(1.77) | 13.51(1.77) | 11.73(5.32) | 13.43(8.85) | 10.80(13.97) | 5.68(25.52) | -0.2(0.3) |
| Intermediate | 18:58:13.02 | +01:40:36.2 | 14.46(1.45) | 12.88(1.30) | 14.53(1.52) | 15.15(1.65) | 7.05(1.09) | 6.22(1.49) | -0.2(0.1) |
| Inner | 18:58:13.04 | +01:40:35.9 | 0.74(0.12) | 0.79(0.10) | 1.82(0.21) | 2.27(0.26) | 2.52(0.26) | 3.08(0.32) | 0.7(0.1) |

NOTE—The intermediate scale corresponds to the extent of the radio jet. Units of right ascension are hours, minutes, and seconds, and units of declination are degrees, arcminutes, and arcseconds.

Table 7. G45.47+0.05: Parameters from Radio Continuum

| Scale | R.A. (J2000) | Dec. (J2000) | S _{5 GHz} (mJy) | S _{41.9 GHz} (mJy) | S _{45.9 GHz} (mJy) | Spectral Index |
|--------------|-----------------|-----------------|-----------------------------|--------------------------------|--------------------------------|-------------------|
| SOMA | 19:14:25.67 | +11:09:25.4 | 58.00(13.52) | 140.10(45.80) | 157.21(78.91) | 0.4(0.2) |
| Intermediate | ... | ... | ... | ... | ... | ... |
| Inner | 19:14:25.67 | +11:09:25.9 | 91.00(9.75) | 102.90(11.27) | 119.70(13.05) | 0.1(0.1) |

NOTE—The quoted flux at 5 GHz is from [Urquhart et al. \(2009\)](#). The quoted fluxes at the inner scale for the higher frequencies correspond to the southern source. Units of right ascension are hours, minutes, and seconds, and units of declination are degrees, arcminutes, and arcseconds.

Table 8. IRAS 20126+4104: Parameters from Radio Continuum

| Scale | R.A. (J2000) | Dec. (J2000) | S _{4.9 GHz} (mJy) | S _{7.4 GHz} (mJy) | S _{20.9 GHz} (mJy) | S _{25.5 GHz} (mJy) | Spectral Index |
|--------------|-----------------|-----------------|-------------------------------|-------------------------------|--------------------------------|--------------------------------|-------------------|
| SOMA | 20:14:26.05 | +41:13:32.5 | 0.37(0.54) | 0.50(0.75) | 0.29(1.49) | 1.13(2.76) | 0.2(1.9) |
| Intermediate | ... | ... | ... | ... | ... | ... | ... |
| Inner | 20:14:26.03 | +41:13:32.5 | 0.06(0.02) | 0.08(0.02) | 0.64(0.07) | 0.85(0.09) | 1.8(0.1) |

NOTE—Units of right ascension are hours, minutes, and seconds, and units of declination are degrees, arcminutes, and arcseconds.

Table 9. Cepheus A: Parameters from Radio Continuum

| Scale | R.A. (J2000) | Dec. (J2000) | S _{1.5 GHz} (mJy) | S _{4.9 GHz} (mJy) | S _{8.3 GHz} (mJy) | S _{14.9 GHz} (mJy) | S _{23.1 GHz} (mJy) | S _{43.0 GHz} (mJy) | Spectral Index |
|--------------|-----------------|-----------------|-------------------------------|-------------------------------|-------------------------------|--------------------------------|--------------------------------|--------------------------------|-------------------|
| SOMA | ... | ... | ... | ... | ... | ... | ... | ... | ... |
| Intermediate | 22:56:17.98 | +62:01:49.4 | 3.40(0.10) | 7.50(0.10) | 9.80(0.10) | 15.80(0.20) | ... | 35.00(2.00) | 0.66(0.01) |
| Inner | 22:56:17.99 | +62:01:49.6 | ... | ... | 6.85(0.07) | ... | 18.50(0.30) | 65.00(0.50) | 1.38(0.01) |

NOTE—The parameters shown in the table are from [Rodríguez et al. \(1994\)](#) and [Curiel et al. \(2006\)](#) for the intermediate and the inner scale, respectively. Units of right ascension are hours, minutes, and seconds, and units of declination are degrees, arcminutes, and arcseconds.

Table 10. NGC 7538 IRS9: Parameters from Radio Continuum

| Scale | R.A. (J2000) | Dec. (J2000) | S _{5.3 GHz} (mJy) | S _{6.3 GHz} (mJy) | S _{41.9 GHz} (mJy) | S _{45.9 GHz} (mJy) | Spectral Index |
|--------------|-----------------|-----------------|-------------------------------|-------------------------------|--------------------------------|--------------------------------|-------------------|
| SOMA | 23:14:01.77 | +61:27:19.8 | 5.00(1.68) | 25.74(5.46) | 2.47(103.89) | <515.49 | <1.1 |
| Intermediate | ... | ... | ... | ... | ... | ... | ... |
| Inner | 23:14:01.76 | +61:27:19.8 | 0.42(0.04) | 0.48(0.06) | 2.50(0.29) | 2.47(0.29) | 0.8(0.1) |

NOTE—Units of right ascension are hours, minutes, and seconds, and units of declination are degrees, arcminutes, and arcseconds.

4. RESULTS

In this paper, a radio detection is defined when the peak intensity I_ν is ≥ 5 times the image rms (σ) in either of the baseband-combined images (see §2.1) at the different bands (i.e., *C*-, *K*- or *Q*-band). For non-detections in one of the combined images we report a 3σ limit value for the flux density at the given frequency. Figure 1 shows VLA contour plots of the *C*-band: 6 cm (red), *K*-band: 1.3 cm (magenta) and *Q*-band: 0.7 cm (blue) combined images toward all the radio sources detected in our sample and overlaid to *SOFIA*-FORCAST $37\mu\text{m}$ images. The blue circles represent the SOMA apertures set from $70\mu\text{m}$ images (except for region IRAS 07299–1651 where the aperture radius is set from the $37.1\mu\text{m}$ image) reported by [DLT17](#) and used to build their IR SEDs (see [DLT17](#) Table 2). The astrometric accuracy of the infrared images presented in [DLT17](#) (including *SOFIA*, *Herschel* and *Spitzer* data) and the VLA data presented here are better than $0''.5$ and $0''.1$ (see Table 2), respectively.

Table 11. SOMA and Intermediate Scales

| Region | SOMA R (") | Intermediate w (") × h (") |
|-----------------|---------------|-------------------------------|
| AFGL 4029 | 11.2 | 3.37 × 1.27 |
| AFGL 437 | 3.84 | ... |
| IRAS 07299–1651 | 7.7 | ... |
| G35.20–0.74 | 32.0 | 3.36 × 16.15 |
| G45.47+0.05 | 14.4 | ... |

Table 11 continued on next page

Table 11 (*continued*)

| Region | SOMA | Intermediate |
|-----------------|-------|------------------|
| | R (") | w(") × h(") |
| IRAS 20126+4104 | 12.8 | ... |
| Cepheus A | 48.0 | ... ^a |
| NGC 7538 IRS9 | 25.6 | ... |

^a Size changes with frequency and they are reported in [Rodríguez et al. \(1994\)](#) Table 1.

NOTE—The reported values correspond to a circle of radius R for the SOMA scale and a box of height h and width w for the intermediate scale.

Tables 3 to 10 report the radio parameters for each of the eight regions studied in this paper. These parameters were measured based on different size scales as follows. The *SOMA* scale refers to the size of the aperture radius used by [DLT17](#) to measure their IR fluxes (except for source AFGL 437; see below). The *Intermediate* scale is based on the morphology of the radio source, specifically if the detections appear of jet-like nature. The *Inner* scale is given by the size of the central radio detection that is likely most closely associated with the driving protostar (i.e., association with compact millimeter dust continuum emission). For the presented VLA data we determined the flux density S_ν in each wide band image in the *SOMA* scale and in the *Intermediate* scale by using the task `imstat` of CASA either enclosing the SOMA aperture in a circular region or enclosing the elongated jet-like structure in a box, respectively (see Table 11). The uncertainties of the flux density for these two scales are estimated as $\sigma_{image}(npts/beamarea)^{0.5}$ added in quadrature with an assumed 10% error in calibration, where σ_{image} is the rms of the image, $npts$ is the number of pixels enclosed in the box or the circular region and the *beam area* is the number of pixels within a synthesized beam of the image. For the *Inner* scale we determined the flux density using the task `imfit` of CASA, and the uncertainty was estimated using the statistical error from the Gaussian fit added in quadrature with an assumed 10% error in calibration.

Tables 3 to 10 column 1 show the given scale and for each scale columns 2 and 3 report the R.A. and decl., which for the *SOMA* scale they refer to the pointing center observations of *SOFIA-FORECAST* (see [DLT17](#) Table 1), for the *Intermediate* scale they refer to a middle point in the jet-like detection and for the *Inner* scale they refer to the R.A. and decl. of the peak intensity of the central detected object. The following columns are the flux densities (S_ν) at different frequencies with the uncertainties given in parentheses, and the last columns in Tables 3 to 10 report the spectral indices and their uncertainties at each scale (see §4.2). Since the radio data are not sensitive to extended emission over scales as large as the *SOMA* and possibly the *Intermediate* scales, the flux measurements represent the sum over all compact sources within the scale and the spectral indices contain some corresponding uncertainty. The error bars for these measurements are large due to having many independent beams within the scale.

4.1. Morphology and Multiplicity

All the target regions presented in this paper have been detected in cm continuum and we describe their morphology as either compact if the detection shows no structure on the scale of a few synthesized beams or extended otherwise. Below we describe the centimeter wavelength detections toward each target; for a detailed background on each of these regions see [DLT17](#).

4.1.1. AFGL 4029

AFGL 4029 is composed of two mid-IR sources, IRS1 and IRS2, with the former being the source of interest in this work. In our data we detected at least four centimeter continuum sources at C-band and one at Q-band, being the eastern and central sources with 5σ detections (also reported by [Zapata et al. 2001](#)) and the two western ones being 3σ detections. We detected only one of the sources of the binary system found by [Zapata et al. \(2001\)](#) at 3.6 cm (named by them as G138.295+1.555 S and located at RA(J2000)=03^h01^m31^s.273, Dec(J2000)= +60°29'12".80) even though our observations have ~ 2 times higher sensitivity and a similar resolution ($\sim 0''.3$) as theirs. This may be further indication that the source G138.295+1.555 N (not detected in our analyzed data), which they reported to be at a separation of $\sim 0''.6$ (or 1200 au at the distance of the region) from G138.295+1.555 S, is a variable radio source, as also suggested by [Zapata et al. \(2001\)](#).

Moreover, we detected the extended east-west fainter emission that they interpreted as being part of an ionized jet that is emanating from G138.295+1.555 S (our detected radio source at the Inner scale) based on the morphology and their alignment

with larger scale outflows (e.g., optical jet: [Ray et al. 1990](#) and CO molecular outflow: [Ginsburg et al. 2011](#)). [Zapata et al. \(2001\)](#) reported a flux density of ~ 0.25 mJy at 3.6 cm for G138.295+1.555 S and detected it as an unresolved source at a resolution of $\sim 0''.3$. The presented data provide further evidence that this system corresponds to an ionized jet (with a projected length of ~ 5000 au) based on the morphology, weak cm continuum emission and a spectral index $\alpha \sim 0.7$, which is consistent with the typical spectral index of ionized jets (e.g., [Reynolds 1986](#); [Anglada et al. 1998](#); [TTZ16](#)). Additionally, although the three other components of the jet (eastern and western components) are not detected at Q-band, probably due to a lack of sensitivity at that band, our upper limit estimates of their spectral indices ($\alpha \lesssim 1$) are still consistent with the expected values for ionized jets.

4.1.2. AFGL 437

AFGL 437 is an infrared star-forming region composed of at least four IR sources (e.g., [Wynn-Williams et al. 1981](#)), where sources AFGL 437W and AFGL 437S have been the only ones reported to be associated with centimeter continuum emission. In our study towards this region, AFGL 437W and AFGL 437S are detected at $> 5\sigma$ as extended and compact radio sources, respectively. Also, for the first time (to the knowledge of the authors) we detected very compact and unresolved centimeter continuum towards the very embedded IR source WK 34 which is associated with AFGL 437N. The position of its peak intensity is RA(J2000)=03^h07^m24^s.571, Dec(J2000)= +58°30'53".00. WK 34 is very weak at 5.8 GHz with a flux density of ~ 60 μ Jy and at 44 GHz it has a flux density of ~ 700 μ Jy, giving a positive spectral index of ~ 1.2 . [Weintraub & Kastner \(1996\)](#) speculated that WK 34 is tracing an outflow cavity and [Kumar Dewangan & Anandaro \(2010\)](#) suggested that WK 34 is a high-mass protostar in an earlier stage than AFGL 437W and AFGL 437S. Therefore, our high-sensitivity observations provide further evidence that high-mass stars even at the earlier stages are associated with very weak thermal radio continuum emission likely associated with ionized jets.

Moreover, a CO molecular outflow roughly oriented N-S has been reported ([Gomez et al. 1992](#); [Qin et al. 2008](#)) towards the center of the IR-emitting region, but it has a very low degree of collimation, perhaps due to the superposition of multiple unresolved outflows ([Manjarrez et al. 2012](#)). AFGL 437W and AFGL 437S have been previously observed at 3.6 cm and 2 cm using the VLA by [Torrelles et al. \(1992\)](#) and [Manjarrez et al. \(2012\)](#) with angular resolutions of $\sim 4''$ and $\sim 1''$, respectively. AFGL 437W is a resolved extended source with an estimated total flux density of ~ 18 mJy at 3.6 cm and ~ 17 mJy at 2 cm and ~ 22 mJy at 3.6 cm and ~ 28 mJy at 2 cm from [Torrelles et al. \(1992\)](#) and [Manjarrez et al. \(2012\)](#), respectively. AFGL 437W appears to be an optically thin UC HII region likely ionized by an early B-type ZAMS star ([Torrelles et al. 1992](#)), although [Manjarrez et al. \(2012\)](#) suggested that this source is a radio jet based on their detected morphology at 2 cm. Since AFGL 437W is resolved and extended, the archival data at 6 cm is missing part of its flux, and the higher resolution data at 0.7 cm are also resolving out this source.

[Torrelles et al. \(1992\)](#) and [Manjarrez et al. \(2012\)](#) estimated a total flux density for AFGL 437S of ~ 1 mJy at 3.6 cm and 2 cm and ~ 1.5 mJy at 3.6 cm and < 2 mJy at 2 cm, respectively. In our data, AFGL 437S appears to be slightly elongated in the NE-SW direction at longer wavelengths and it has a rising spectral index, consistent with [Manjarrez et al. \(2012\)](#), thus AFGL 437S could be either an optically thick UC/HC HII region or an ionized jet. In this study, we test the scenario that AFGL 437S is associated with an ionized jet that is likely undergoing mass loss ([Manjarrez et al. 2012](#)). In order to do so, we have built the SED for AFGL 437S and therefore we do not use the photometry measured by *DLT17* whose SED includes emission from all the four IR sources of the cluster. Our *SOMA* scale for AFGL 437S has a circular aperture of radius $R_{\text{ap}} = 3.84''$ around AFGL 437S and we only use the data at wavelengths $< 40\mu\text{m}$ because at longer wavelengths the source is unresolved. Table 12 has the integrated flux densities for AFGL 437S from the IR data and Table 4 shows our measured total flux density for the centimeter wavelengths archival data.

Table 12. AFGL 437S: Infrared Flux Densities

| Facility | λ (μm) | $F_{\lambda, \text{sub}}^{\text{a}}$ (Jy) | F_{λ}^{a} (Jy) |
|----------------------|--------------------------------|--|----------------------------------|
| <i>Spitzer</i> /IRAC | 3.6 | 0.35 | 0.40 |
| <i>Spitzer</i> /IRAC | 4.5 | 0.71 | 0.78 |
| <i>Spitzer</i> /IRAC | 5.8 | 1.56 | 1.77 |
| SOFIA/FORCAST | 7.7 | 3.13 | 3.89 |
| <i>Spitzer</i> /IRAC | 8.0 | 2.77 | 3.32 |
| SOFIA/FORCAST | 19.7 | 22.37 | 27.09 |

Table 12 continued on next page

Table 12 (*continued*)

| Facility | λ (μm) | $F_{\lambda,b-sub}^a$ (Jy) | F_{λ}^a (Jy) |
|---------------|--------------------------------|-------------------------------|-------------------------|
| SOFIA/FORCAST | 31.5 | 46.27 | 65.10 |
| SOFIA/FORCAST | 37.1 | 53.79 | 76.69 |

^a Flux density derived with a fixed aperture radius of $R_{ap} = 3.84''$ from the $70\mu\text{m}$ data.

NOTE— $F_{\lambda,b-sub}$ and F_{λ} correspond to the flux density derived with and without background subtraction, respectively.

4.1.3. IRAS 07299–1651

IRAS 07299–1651 appears extended in the NIR and MIR, it is associated with methanol maser emission that shows a velocity gradient and evidence of CO outflow wings, and all these tracers share a similar elongation axis in the NW-SE direction (Walsh et al. 1999, 2001).

We present 6 cm observations towards this region where we have detected at least one resolved and slightly elongated source. Also, we detect at least two more unresolved sources that appear aligned with the central source in the E-W direction. However, our resulting images towards this region have calibration errors and the source is very faint for self-calibration, thus we can not rule out that these two sources are image artifacts. The central detection is consistent with the source reported by Walsh et al. (1998) within their absolute positional accuracy ($\sim 1''$) and they reported that it is associated with 6.7 GHz methanol masers. At this point, the nature of IRAS 07299–1651 is unclear: it could be either an UC/HC HII region or an ionized jet. Thus we require additional information such as high resolution centimeter continuum at higher frequencies to further constrain its nature.

4.1.4. G35.20–0.74

Also known as G35.20–0.74N, this region is seen in the infrared as an elongated source oriented N-S that hosts a weakly collimated bipolar CO molecular outflow that extends in the NE-SW direction. This region is associated with at least three hot molecular cores labeled A, B and C which are oriented in the NW-SE direction (Sánchez-Monge et al. 2014). Centimeter continuum observations (e.g., Gibb et al. 2003) have revealed the presence of a string of radio sources that are coincident with the N-S elongated IR emission seen in the region. Recently, Beltrán et al. (2016) detected 17 centimeter continuum sources at angular resolutions of $\sim 0''.4 - \sim 0''.05$ (some of these data are also used in our study) towards G35.20–0.74 and based on the spectral indices of each component found that core B is associated with an UC/HC HII region (their source 8a) that is part of a young binary system ($\sim 0''.37$ apart) and it is likely driving an ionized jet oriented N-S (with a projected length of $\sim 33,000$ au). Beltrán et al. (2016) proposed that most of the radio sources detected are part of the ionized jet and based on their spectral indices, some of the emission of these knots is non-thermal. The ionized jet is expanding at a velocity of ~ 300 km s⁻¹ and appears to be precessing as suggested by its S-shaped morphology and the misalignment with respect to the larger scale CO molecular outflow (Beltrán et al. 2016). Cores A and C are also associated to UC/HC HII regions and are inside our *SOMA* scale: hence the higher flux densities measured at this scale. However, we also measure a high flux density at our *Intermediate* scale compared with the *Inner* scale.

4.1.5. G45.47+00.05

G45.47+00.05 appears as a resolved and slightly elongated radio continuum source (e.g., Urquhart et al. 2009; Towner et al. 2017), associated with at least one molecular outflow roughly oriented with a N-S axis (Wilner et al. 1996). Wood & Churchwell (1989) observed this source at 6 cm with an angular resolution of $\sim 0''.4$ and cataloged it as an irregular UC HII region, since their observations revealed a NE-SW elongation as well as a slight NW-SE elongation. Wilner et al. (1996) studied the centimeter continuum spectrum of G45.47+00.05 and suggested that it was consistent with a partially ionized stellar wind. Additionally, Towner et al. (2017) presented VLA 1.3 cm observations estimating a flux density of ~ 180 mJy with an angular resolution of $\sim 1''$ that also revealed an elongated morphology along the NW-SE axis, suggesting an ionized jet nature. In this work we present very high resolution ($\sim 0''.04$) VLA Q-band archival data where we can see for the first time (to the knowledge of the authors) that G45.47+00.05 is fragmented into at least two centimeter continuum sources $\sim 0''.4$ apart (or ~ 3400 au at the distance of G45.47+00.05). The southern source, which we have named G45.47+00.05S, is very bright at 43.9 GHz with a flux density of ~ 110 mJy, appears slightly elongated along the N-S axis and its peak intensity position at that frequency

is RA(J2000)= $19^h 14^m 25^s.677$, Dec(J2000)= $+11^\circ 09' 25''.56$. The northern source, which we have named G45.47+00.05N, is weaker at 43.9 GHz with a flux density of ~ 20 mJy, has a jet-like morphology elongated in the E-W axis and its peak intensity position at that frequency is RA(J2000)= $19^h 14^m 25^s.683$, Dec(J2000)= $+11^\circ 09' 25''.96$. Our *Inner* scale is centered around G45.47+00.05S at Q-band where the source is resolved.

4.1.6. IRAS 20126+4104

IRAS 20126+4104 has infrared emission that is slightly elongated along the same NW-SE axis as the associated bipolar molecular outflow (e.g., [Cesaroni et al. 1997](#)). [Rosero et al. \(2016\)](#) detected at least five centimeter continuum sources that are within our SOMA aperture as seen in Figure 1. [Hofner et al. \(2007\)](#) suggested that the central, slightly elongated sources seen in Figure 1 correspond to two collimated ionized jets, one of them composed of radio sources N1 and N2 and the second ionized jet known as source S. It has been suggested that source N1 sits at the origin of the larger scale molecular outflow and also appears to be surrounded by a nearly Keplerian and stable accretion disk (e.g., [Cesaroni et al. 2014](#); [Chen et al. 2016](#)). Additionally, [Hofner et al. \(2007\)](#) reported that the southern radio source towards IRAS 20126+4104 (labeled I20var) is a variable radio source, consistent with gyrosynchrotron emission from a T-Tauri star. I20var is located $\sim 5''.0$ to the SE of source N1. The other two sources found by [Rosero et al. \(2016\)](#) were labeled source C (located $\sim 4''.0$ NW apart from N1) and G78.123+3.629 (located $\sim 11''.5$ SE apart from N1, very near to the edge of the millimeter dust core) and are new detections with reported spectral indices that are consistent with non-thermal emission. It is possible that at the distance of IRAS 20126+4104 the VLA could still detect low-mass stars ([Rosero et al. in prep](#)), thus these non-thermal highly variable radio sources could be flaring T-Tauri stars. In this scenario, IRAS 20126+4104 would be a small multiple system of two high-mass protostars surrounded by at least three pre-main sequence low-mass stars. The four central sources are within a projected radius of $\sim 4''.5$ (7400 au at the distance of IRAS 20126+4104).

4.1.7. Cepheus A

Cepheus A is a well known star-forming region and it is seen in the infrared as an elongated source oriented NE-SW. This region is the host of a complex multipolar CO molecular outflow that is likely powered by a small cluster of deeply embedded protostars (e.g., [Curiel et al. 2006](#); [Zapata et al. 2013](#)). Our SOMA aperture encloses the whole Cepheus A East region that is composed of several centimeter continuum sources as seen in [Zapata et al. \(2013\)](#). The brighter centimeter continuum source found towards this region, known as HW2, is an ionized thermal jet oriented NE-SW and it is thought to be the main driver of the complex outflow activity in Cepheus A and to contribute at least half of the total luminosity of the region (e.g., [Zapata et al. 2013](#)). Also, the ionized jet in HW2 is associated and aligned with a bipolar HCO⁺ molecular outflow ([Gómez et al. 1999](#)). [Curiel et al. \(2006\)](#) resolved the Cepheus A HW2 ionized jet at 3.6 cm in three radio sources, where HW2 is the central powering source and the NE and SW sources are knots along the jet that are moving away from HW2 at a velocity of ~ 500 km s⁻¹. Based on maser and millimeter observations some authors have suggested that HW2 has an associated circumstellar disk (e.g., [Patel et al. 2005](#); [Sugiyama et al. 2014](#); [Sanna et al. 2017](#)). We used the reported values from [Curiel et al. \(2006\)](#) with angular resolutions of $\sim 0''.27$ and $\sim 0''.05$ for the central source for our study of the *Inner* scale. We used the reported values from [Rodriguez et al. \(1994\)](#) of the radio jet for our study of the *Intermediate* scale. We are not analyzing the SOMA aperture towards this region due to a lack of a complete suit of observations that enclosed all the radio sources at this scale.

4.1.8. NGC 7538 IRS9

NGC 7538 IRS9 is part of a cluster of infrared regions that host several high-mass star forming cores. [Sandell et al. \(2005\)](#) detected a faint and marginally resolved radio source (known as IRS 9) in this region using VLA data at angular resolution of $\sim 1''$ at 3.6 cm and 6 cm and with a rms noise of $60 \mu\text{Jy beam}^{-1}$ and $100 \mu\text{Jy beam}^{-1}$, respectively. Based on their measured spectral index they have suggested that IRS 9 is free-free emission from an ionized jet, a scenario that is consistent with the observed collimated, compact and bipolar HCO⁺ molecular outflow that is centered on IRS 9 and oriented E-W. [van der Tak & Menten \(2005\)](#) detected IRS 9 using VLA data at 43.3 GHz at two angular resolutions of $\sim 0''.5$ and $\sim 0''.05$. Our results show further evidence that the radio emission from IRS 9 is dominated by free-free emission. Additionally, from these archival observations we have detected a new weak and unresolved radio source at 5.8 GHz, located $\sim 1''.8$ NE from IRS9 (or ~ 4800 au). This new radio detection has a flux density at 5.8 GHz of ~ 0.2 mJy, and its peak intensity position is RA(J2000)= $23^h 14^m 01^s.844$, Dec(J2000)= $+61^\circ 27' 21''.46$. This source appears to be undetected by the observations of [Sandell et al. \(2005\)](#), which suggests that this newly detected radio source may be a radio variable source or that their observations lacked the angular resolution to distinguish these two sources. We estimate an upper limit on the radio spectrum for this new component which is consistent with a flat or even a negative spectral index.

4.2. Radio SEDs

In Figure 2 we present the centimeter SEDs for our regions. The dashed lines are the best fit to the data of a power law of the form $S_\nu \propto \nu^\alpha$, where α is the spectral index, derived at the different scales: “SOMA”, “Intermediate” and “Inner”, as described above. The spectral index was calculated using the flux density at the central frequencies from the images (and/or the available data in the literature), thus α is calculated over a wide frequency range (>20 GHz), except for IRAS 07299–1651 where we only have data at 6 cm. The presented archival data were observed at different angular resolutions at different frequencies, with the lower frequency observed (C-band: 6 cm) at a resolution around 10 times lower than the higher frequency (Q-band: 0.7 cm). This is not a major concern for sources measured to be very compact or unresolved at C-band because they will then be smaller than the largest angular scale for which the Q-band observations are sensitive. For the sources in this study (typically at about 2 kpc) this corresponds to a linear size of ~ 2400 au.

However, more extended sources may suffer from resolution bias and/or lack of short spacing data (resolved out), affecting our ability to recover a source’s entire flux. Additionally, at the higher frequencies (K-band and Q-band in our study) the fluxes are most likely measuring the combination of dust and free-free emission (see Brogan et al. 2016). We assume that the fluxes at Q-band are an upper limit on the free-free emission contribution. The uncertainty in the spectral index was calculated with a Monte Carlo simulation that bootstrapped the flux density uncertainties. We estimated an upper limit in the spectral index for non-detections at higher frequencies using a value of S_ν of 3σ .

5. ANALYSIS

The centimeter continuum emission associated with the regions located at distances >1 kpc have low radio fluxes (<3 mJy) in our *Inner* scale, except for G45.47+0.05. The analyzed data do not allow us to make a systematic study of the nature of this detected emission, but we favor the speculation from previous studies that some of them are part of a protostellar jet/wind, at least based on their morphology, as in the case of AFGL 4029, G35.20–0.74, IRAS 20126+4104. Cepheus A is the only region in this study located at a distance <1 kpc and it is one of the best examples of a collimated ionized jet from a high-mass protostar in the literature (Rodríguez et al. 1994).

Figure 3 shows the extended spectral energy distributions, i.e., including radio fluxes as well as the infrared fluxes from DLT17, for our eight sources. The solid colored lines (except yellow ones) correspond to the best five models obtained from the ZT protostellar radiative transfer models. As explained in DLT17, the data at $\lesssim 8 \mu\text{m}$ are considered to be upper limits since PAH emission and transiently heated small grain emission are not well treated in the ZT models.

In the cases of AFGL 4029 and IRAS 20126+4104, all of the best five models have a higher predicted radio flux than what is observed. In these cases, we analytically select alternative models within the top 20 models from the IR fitting and that are expected to have lower radio fluxes. In general, the free-free flux quickly increases when the photoionized region breaks out the inner disk wind. Therefore, we selected alternative models that are expected to be just before the break-out phase, which is typically at the protostellar mass of $m_* \simeq 10 (\dot{m}_*/10^{-4} M_\odot \text{yr}^{-1})^{0.28} M_\odot$ (TTZ16; Tanaka et al. 2017). Ultimately, as in the ZT model for IR and sub-mm wavelengths, we aim to prepare a full suite of model grids for centimeter wavelengths, but since this is computationally expensive we defer it to a future paper.

The parameters of the best-fit ZT models are listed in Table 13 but now ordered from best to worst as measured by the reduced χ^2 from the inner scale ($\chi_{all_inner}^2$). This is because the ZT and TTZ16 models are developed assuming a single protostar within a core and with a focus on the inner regions. The reduced χ^2 is estimated using equation 4 from Zhang & Tan (2018). The radio data occurring within the same band (i.e., with very similar frequencies) were averaged together to give more equal weight over the SED.

5.1. Comparing models with data

We now describe the results of the TTZ16 models for each of the eight regions using the best five models from the ZT grid as examples, except for AFGL 4029 and IRAS 20126+4104 where we had to identified a best overall model from the ZT results that is beyond the best five (but within the best 20 results). We center our attention on the results from the *Inner* scale since the TTZ16 model assumes that a prestellar core collapses to form a single high-mass star and it is mostly focussed on the inner regions.

AFGL 4029: The best two fit models using MIR to FIR data alone to build the SED have $\chi_{IR}^2 = 1.07$ and 1.16 and have parameters of protostellar mass $m_* = 12$ and $48 M_\odot$, core mass $M_c = 30$ and $160 M_\odot$ and $\Sigma_{cl} = 0.3$ and 1 g cm^{-2} clumps, respectively. Including the centimeter continuum fluxes to better cover the SED we can see in Figure 3 that the best five models seem to be overestimating the expected free-free emission by ~ 1 dex. Therefore, after exploring other resulting models from the DLT17 study, we found a matching model with $\chi_{IR}^2 = 1.74$ and $\chi_{all_inner}^2 = 11.07$, which yields protostellar parameters of $m_* = 8 M_\odot$, a relatively low mass of the core ($M_c = 80 M_\odot$) and $\Sigma_{cl} = 0.1 \text{ g cm}^{-2}$, accreting at $5 \times 10^{-5} M_\odot \text{yr}^{-1}$ and a bolometric luminosity of $\sim 10^4 L_\odot$.

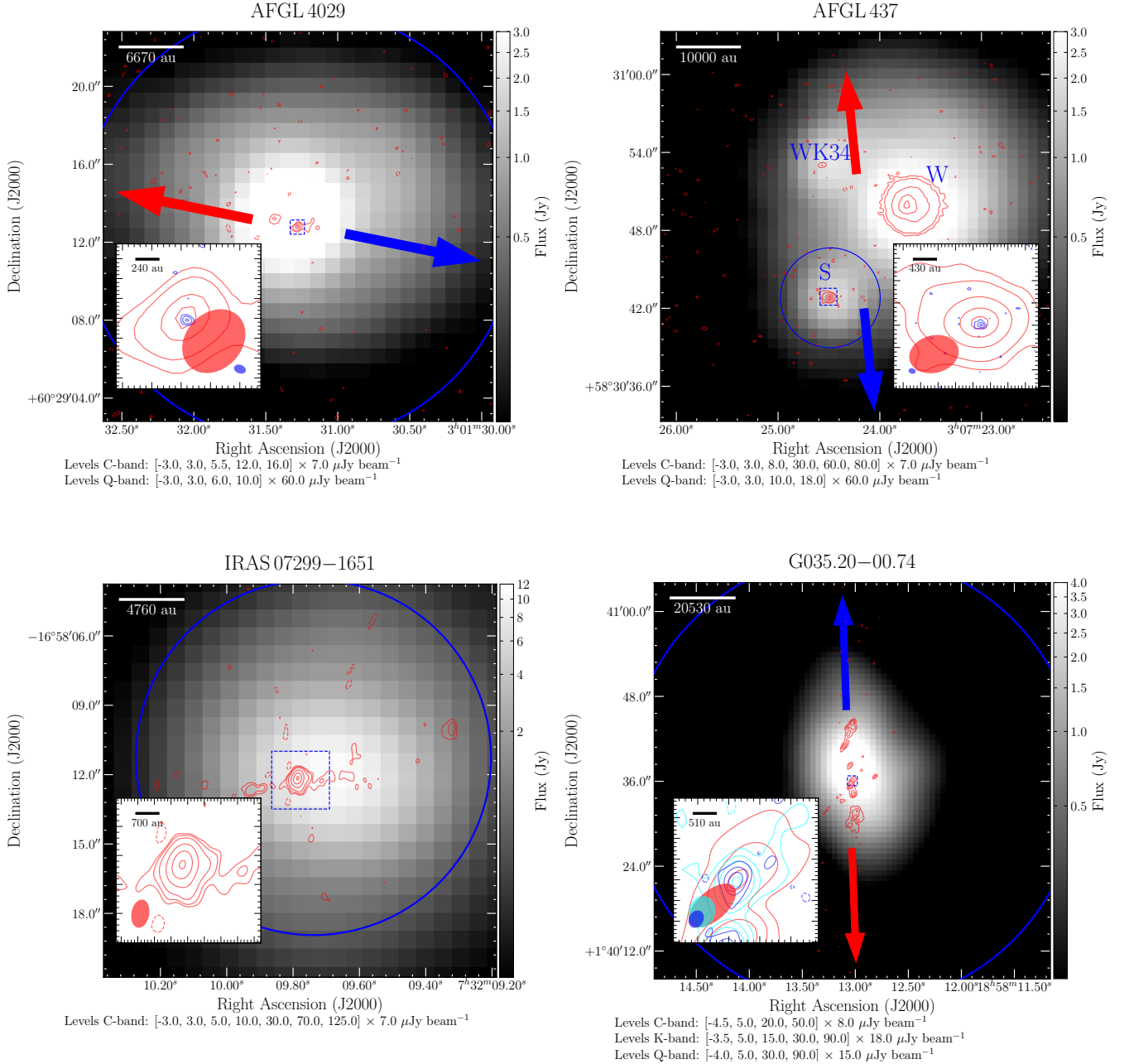


Figure 1. Images are SOFIA-FORCAST 37 μ m with VLA contours –red: C-band (6 cm); magenta: K-band (1.3 cm); blue: Q-band (0.7 cm)– of the combined radio maps overlaid. Contours in Cepheus A are 8.3 GHz and 42.9 GHz from [Curiel et al. \(2006\)](#), see their Figure 2 for a higher resolution image of these contours) and the location and size of this inset are represented by the small blue box shown towards the region. The dashed squares correspond to the area of the inset image showing a zoom in of the central region and the synthesized beams are shown in the lower corners of these insets. The blue circles are the SOMA apertures used by [DLT17](#) and reported in their Table 2 (aperture radius defined from 70 μ m emission except for IRAS07299–1651 where it is set at 37.1 μ m). The blue and red arrows represent the direction of a molecular outflow detected towards the region. A scale bar in units of au is shown in the upper left of the figures.

AFGL 437S: For source AFGL 437S we lack reliable FIR measurements at wavelengths >40 μ m (see above) and we have only three effective data points (plus the 3–8 μ m data treated as upper limits), thus the results from the ZT models in this case are not that well constrained. In this specific case we benefit greatly from the centimeter emission to refine our results. The best-fit model using MIR data alone has $\chi^2_{\text{IR}} = 0.04$ and produces parameters of $m_* = 2M_{\odot}$, a core of mass $M_c = 10M_{\odot}$ and $\Sigma_{\text{cl}} = 3.2$ g cm⁻² clump. However, we disfavor this model since from the radio observations it is obvious that this source has a temperature high enough to emit UV photons that has already formed an UC/HC HII region. Therefore, our best matching model as based on

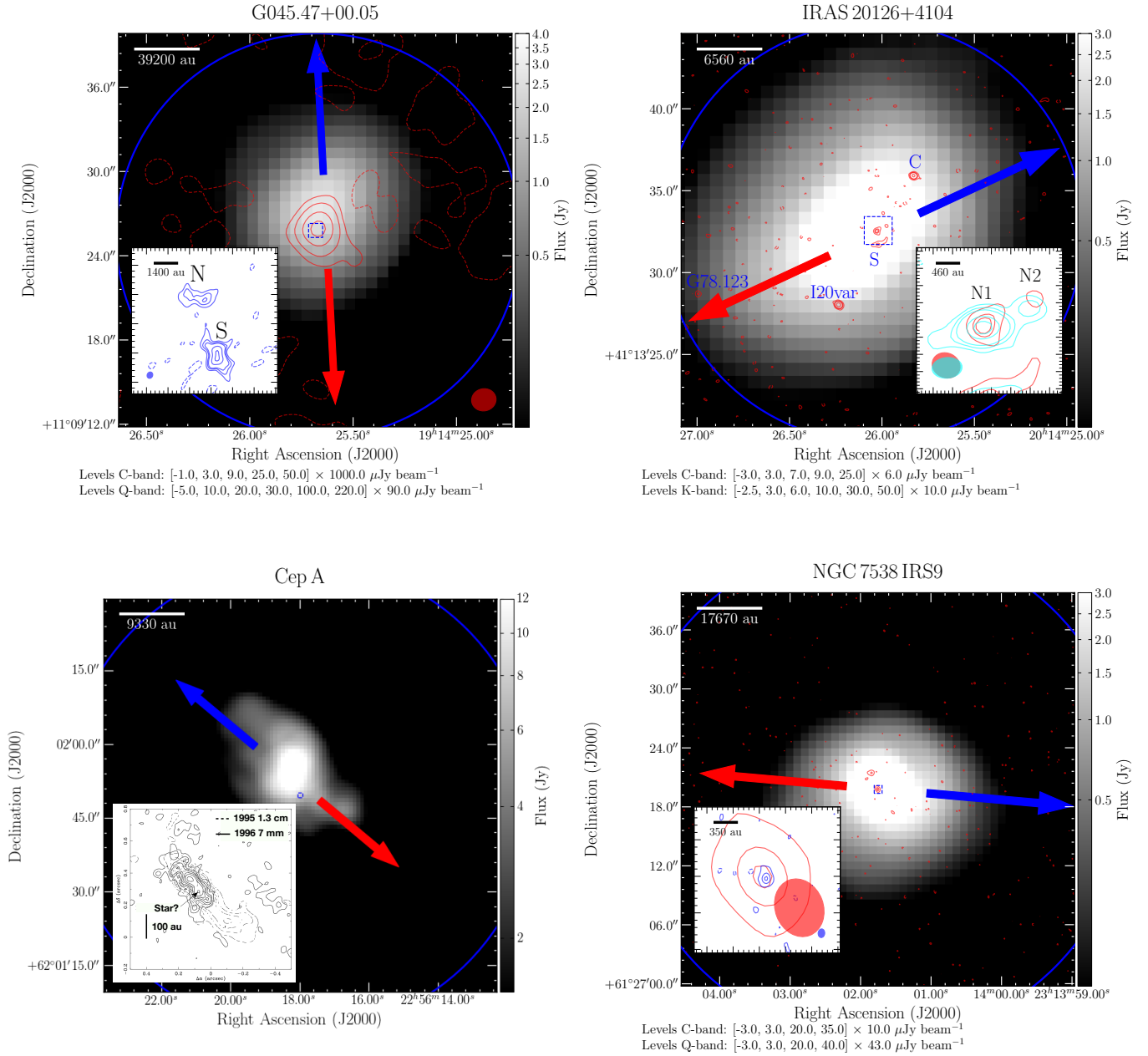


Figure 1. Continued.

the $\chi_{IR}^2 = 0.29$ and $\chi_{all_inner}^2 = 4.52$ has $m_\star = 12M_\odot$, a core of mass $M_c = 50M_\odot$ and $\Sigma_{cl} = 0.1 \text{ g cm}^{-2}$ clump. These parameters are also more consistent with the ones reported by Kumar Dewangan & Anandarao (2010).

IRAS 07299-1651: This source also has a relatively limited amount of data in the FIR and in the centimeter to constrain the models. The best-five ZT models using only the IR data indicate that a protostar in the range of 8–16 M_\odot , in relatively low- Σ clumps and mainly in cores of more than a couple hundred solar masses can fit well the observations. When including our centimeter wavelength emission for this source, our best matching model has $\chi_{IR}^2 = 0.90$ and $\chi_{all_inner}^2 = 3.46$ with parameters of $m_\star = 12M_\odot$, a core of mass $M_c = 240M_\odot$ and a $\Sigma_{cl} = 0.1 \text{ g cm}^{-2}$ clump. A similar fit is given by the second best model based on the $\chi_{all_inner}^2 = 3.54$ with the only difference being the mass of the core is slightly lower.

G35.20-0.74: The best-fit model using the IR SED alone also corresponds to the best matching model when adding the centimeter data emission with $\chi_{IR}^2 = 2.60$ and $\chi_{all_inner}^2 = 19.35$ with parameters of $m_\star = 16M_\odot$, a core of mass $M_c = 480M_\odot$ and

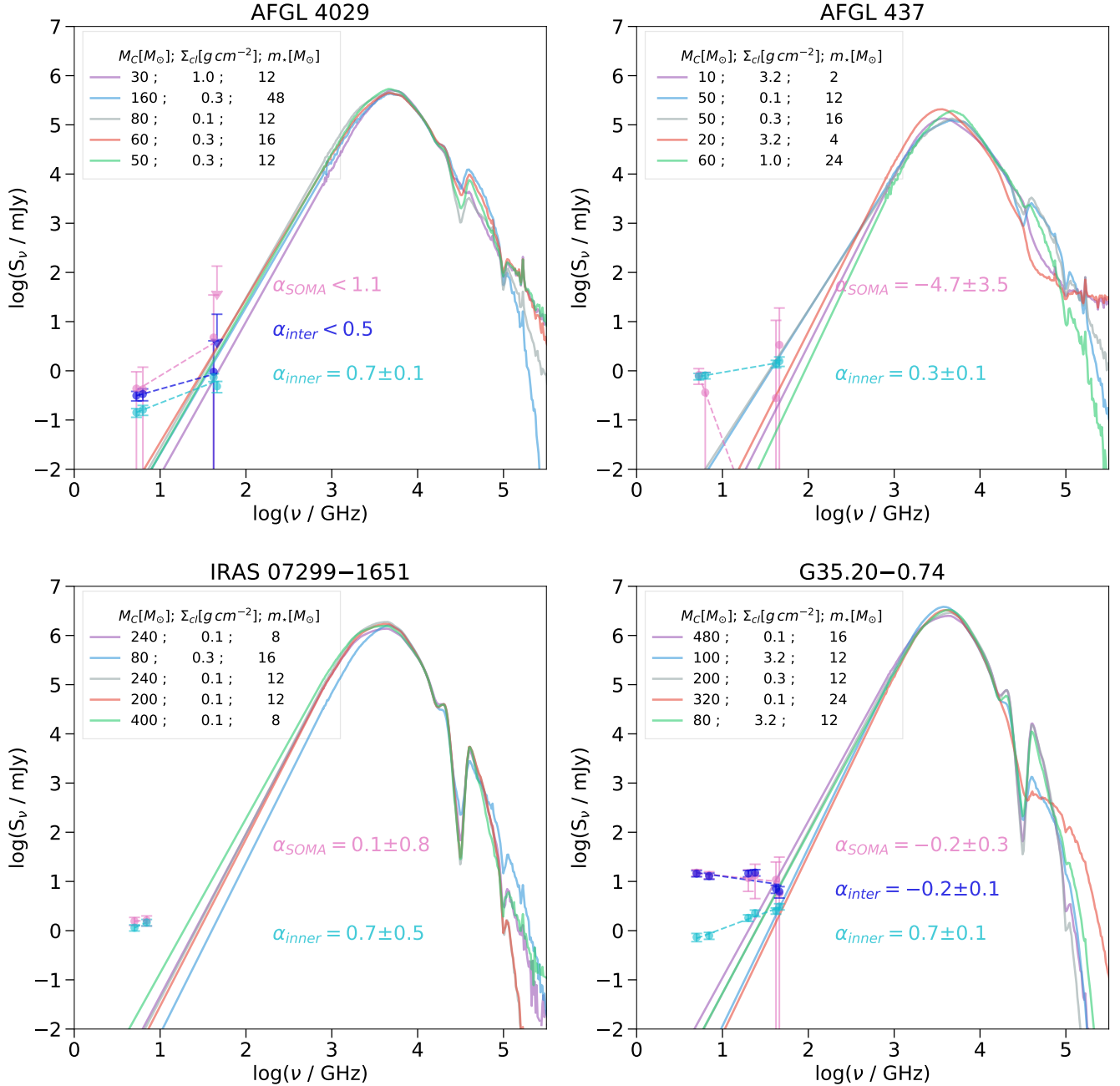


Figure 2. Observed radio spectral energy distributions of SOMA protostars. The circles correspond to the flux density as a function of frequency for each scale (magenta: SOMA; blue: Intermediate; cyan: Inner). Error bars are explained in §4.2. The dashed lines are the best fit to the data from a power law of the form $S_\nu \propto \nu^\alpha$. The solid lines show the best five IR SED ZT models as fit by DLT17 (see legend).

a $\Sigma_{cl} = 0.1 \text{ g cm}^{-2}$ clump. The source detected at the *Inner* scale (or source 8a in Beltrán et al. 2016) is slightly extended at 6 cm and it is blended with other components, however it is a point source at 1.3 cm and 0.7 cm. Thus, it is possible then that we are missing part of the flux at 6 cm and this may explain why the models seem to overestimate the expected free-free emission at 6 cm. Our resulting protostellar mass of $16 M_\odot$ is consistent with the value of $18 M_\odot$ estimated by Sánchez-Monge et al. (2013) when fitting the velocity field of the core with a rotating Keplerian disk, although they argue that this value corresponds to the total mass of a binary system in core B. Our results disfavor the models with protostellar mass $m_* = 12 M_\odot$ and with relatively low core masses and high Σ_{cl} clumps, since the expected free-free emission for these models is many orders of magnitude lower than the observed one.

G45.47+00.05: The observed centimeter continuum emission from G45.47+00.05S (which is the dominant source in the region) is significantly higher (by a few orders of magnitude) than the predicted free-free emission from any of our IR-derived

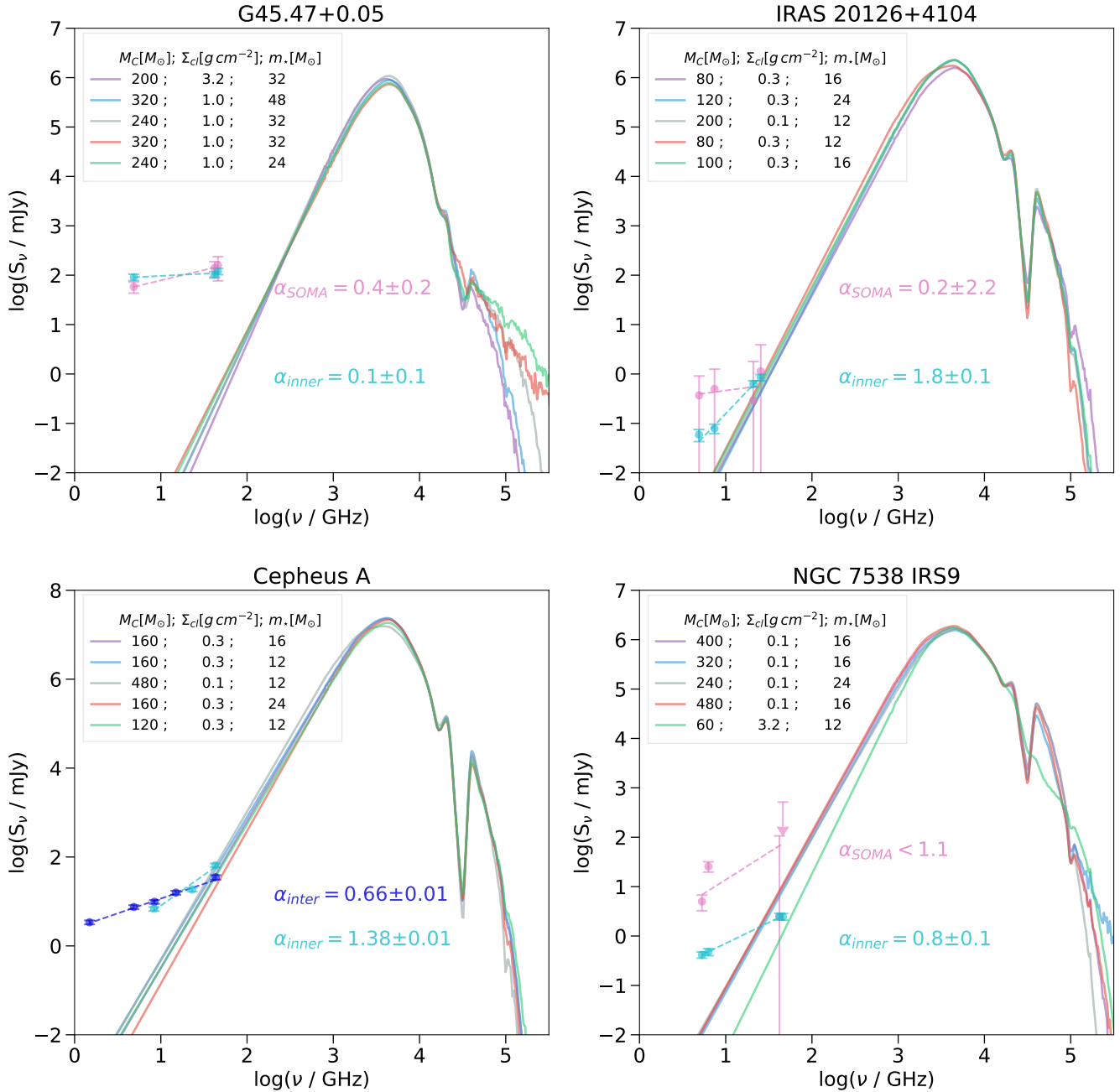


Figure 2. Continued.

ZT models. This is despite the fact that the best two models from the ZT results are already predicting a rather high-mass protostar in the range of $30\text{--}50 M_\odot$ embedded in a massive core, a relatively high Σ clump and low accretion rates in the range of $\sim 10^{-5} M_\odot \text{yr}^{-1}$. Among the eight sources presented in this study this is the only case where none of the free-free models can describe the centimeter emission observed in the source. This region is also the most luminous and likely the most evolved one in this sample, which leads us to think that the radio emission from this source may be boosted by the process of photoevaporation. Photoevaporation is not yet accounted for in the TTZ model, which only considered photoionization of the magnetocentrifugally-driven wind. However, as the protostar increases its mass above $\sim 20 M_\odot$, the ionizing radiation becomes dramatically stronger, creating a photoevaporation flow from the disk and infall envelope that is exposed by the outflow cavity wall, i.e., a wind driven by ionized gas-pressure. By enhancing the mass of ionized gas, the centimeter continuum emission is expected to be much higher than that predicted by TTZ model without such a photoevaporation flow.

IRAS 20126+4104: Including the centimeter continuum fluxes to better sample the SED, we can see in Figure 3 that the best

five models seem to be overestimating the expected free-free emission. Therefore, after exploring other resulting models from the *DLT17* study and the *ZT* models, we found a matching model with $\chi_{IR}^2 = 3.38$ and $\chi_{all_inner}^2 = 5.42$, which yields protostellar parameters of $m_* = 8 M_\odot$, core mass $M_c = 240 M_\odot$ and $\Sigma_{cl} = 0.1 \text{ g cm}^{-2}$. This protostellar mass is consistent with the value of 7–10 M_\odot estimated by [Cesaroni et al. \(2005\)](#); [Moscadelli et al. \(2011\)](#); [Cesaroni et al. \(2014\)](#) from methyl cyanide emission that is likely tracing a Keplerian disk around the protostar. However, with similar methods [Chen et al. \(2016\)](#) estimated a protostellar mass of 12 M_\odot . Therefore either of our best-two models presented in [Table 13](#) for this source could be applicable.

Cepheus A: The best matching model for this source after using the extended SED from centimeter to NIR emission has $\chi_{IR}^2 = 2.43$ and $\chi_{all_inner}^2 = 7.13$ and is constrained to a protostellar mass of $m_* = 12 M_\odot$, a relatively massive core of $M_c = 480 M_\odot$ and a $\Sigma_{cl} = 0.1 \text{ g cm}^{-2}$ clump. Our result is consistent with the kinematic masses estimated for the central source HW2 which are in the range of 10–20 M_\odot (e.g., [Sanna et al. 2017](#)).

NGC 7538 IRS9: Our results using the extended SED favor all our models with a protostellar mass of $m_* = 16 M_\odot$, with a relatively massive core in the range of 320–480 M_\odot and a $\Sigma_{cl} = 0.1 \text{ g cm}^{-2}$ clump. Based on our results, we disfavor the model that has a 12 M_\odot protostar, embedded in a core of $M_c = 60 M_\odot$ and $\Sigma_{cl} = 3.2 \text{ g cm}^{-2}$, since the predicted free-free emission from such model is significantly lower than the observed one.

Table 13. Parameters of the Best-fitted Models of [Zhang & Tan and Tanaka et al. 2016](#)

| Region | $\chi_{all_inner}^2$ | $\chi_{all_inter}^2$ | $\chi_{all_SOMA}^2$ | χ_{IR}^2 | M_c (M_\odot) | Σ_{cl} (g cm^{-2}) | R_c (pc)('') | m_* (M_\odot) | θ_{view} ($^\circ$) | A_V (mag) | M_{env} (M_\odot) | $\theta_{w,esc}$ ($^\circ$) | \dot{M}_{disk} ($10^{-4} M_\odot \text{ yr}^{-1}$) | L_{bol} ($10^4 L_\odot$) |
|-------------|-----------------------|-----------------------|----------------------|---------------|------------------------|---|-------------------|------------------------|---------------------------------|----------------|----------------------------|----------------------------------|---|---------------------------------|
| AFGL 4029 | 11.07 | 1.71 | 1.62 | 1.74 | 80 | 0.1 | 0.21(22) | 8 | 74 | 0.0 | 62 | 27 | 0.5 | 0.97 |
| | 36.87 | 9.03 | 1.51 | 1.36 | 80 | 0.1 | 0.21(21) | 12 | 88 | 0.0 | 47 | 40 | 0.5 | 1.6 |
| | 43.55 | 12.31 | 1.52 | 1.16 | 160 | 0.3 | 0.17(17) | 48 | 88 | 15.2 | 14 | 77 | 1.1 | 0.34 |
| | 51.95 | 16.83 | 1.68 | 1.07 | 30 | 1.0 | 0.04(4) | 12 | 62 | 13.1 | 6 | 53 | 1.9 | 4.1 |
| | 58.35 | 18.29 | 2.16 | 1.55 | 50 | 0.3 | 0.09(10) | 12 | 51 | 15.2 | 22 | 46 | 1.0 | 2.4 |
| | 60.05 | 18.02 | 2.08 | 1.47 | 60 | 0.3 | 0.10(10) | 16 | 62 | 4.0 | 19 | 56 | 1.1 | 3.6 |
| AFGL 437 | 4.52 | ... | 0.42 | 0.29 | 50 | 0.1 | 0.16(17) | 12 | 80 | 7.5 | 15 | 59 | 0.3 | 1.4 |
| | 17.89 | ... | 1.66 | 0.32 | 50 | 0.3 | 0.09(9) | 16 | 77 | 2.6 | 8 | 68 | 0.7 | 3.1 |
| | 49.37 | ... | 5.28 | 0.53 | 60 | 1.0 | 0.06(6) | 24 | 89 | 16.8 | 5 | 71 | 1.9 | 9.3 |
| | 334.54 | ... | 36.74 | 0.51 | 20 | 3.2 | 0.02(2) | 4 | 39 | 0.0 | 12 | 34 | 3.1 | 0.3 |
| | 399.67 | ... | 42.59 | 0.04 | 10 | 3.2 | 0.01(1) | 2 | 39 | 0.0 | 6 | 35 | 1.8 | 0.3 |
| IRAS 07299 | 3.46 | ... | 1.47 | 0.90 | 240 | 0.1 | 0.36(44) | 12 | 89 | 48.5 | 211 | 19 | 0.9 | 2.0 |
| | 3.54 | ... | 1.59 | 1.07 | 200 | 0.1 | 0.33(40) | 12 | 89 | 51.5 | 174 | 20 | 0.8 | 2.0 |
| | 22.65 | ... | 16.42 | 0.62 | 240 | 0.1 | 0.36(44) | 8 | 89 | 6.1 | 226 | 13 | 0.7 | 1.1 |
| | 26.21 | ... | 13.07 | 0.86 | 80 | 0.3 | 0.12(14) | 16 | 89 | 12.1 | 42 | 42 | 1.5 | 4.2 |
| | 70.69 | ... | 46.46 | 1.16 | 400 | 0.1 | 0.47(57) | 8 | 62 | 0.0 | 386 | 10 | 0.8 | 1.0 |
| G35.20–0.74 | 19.35 | 34.03 | 21.00 | 2.60 | 480 | 0.1 | 0.51(48) | 16 | 48 | 40.4 | 440 | 15 | 1.2 | 3.9 |
| | 26.10 | 19.89 | 13.05 | 2.76 | 200 | 0.3 | 0.19(17) | 12 | 22 | 43.4 | 173 | 17 | 1.9 | 4.0 |
| | 33.14 | 15.25 | 9.85 | 2.79 | 80 | 3.2 | 0.04(3) | 12 | 39 | 15.2 | 58 | 22 | 8.4 | 5.0 |
| | 135.79 | 472.57 | 328.48 | 2.62 | 100 | 3.2 | 0.04(4) | 12 | 34 | 28.3 | 77 | 20 | 9.4 | 5.2 |
| | 158.33 | 521.58 | 356.98 | 2.78 | 320 | 0.1 | 0.42(39) | 24 | 68 | 81.8 | 256 | 27 | 1.2 | 8.4 |
| G45.47+0.05 | 40.94 | ... | 9.53 | 1.20 | 200 | 3.2 | 0.06(1) | 32 | 89 | 61.6 | 140 | 25 | 16.9 | 46.0 |
| | 57.05 | ... | 12.91 | 1.33 | 320 | 1.0 | 0.13(3) | 48 | 89 | 46.5 | 200 | 35 | 9.3 | 50.9 |
| | 68.80 | ... | 15.74 | 1.68 | 320 | 1.0 | 0.13(3) | 32 | 68 | 15.2 | 252 | 24 | 8.2 | 27.4 |
| | 71.24 | ... | 16.22 | 1.62 | 240 | 1.0 | 0.11(3) | 32 | 83 | 2.0 | 170 | 30 | 7.2 | 25.7 |
| | 79.60 | ... | 18.14 | 1.71 | 240 | 1.0 | 0.11(3) | 24 | 55 | 0.0 | 192 | 23 | 6.6 | 17.2 |
| IRAS 20126 | 5.42 | ... | 2.99 | 3.38 | 240 | 0.1 | 0.36(45) | 8 | 71 | 24.2 | 226 | 13 | 0.7 | 1.0 |
| | 53.82 | ... | 2.48 | 2.38 | 80 | 0.3 | 0.12(15) | 12 | 44 | 73.7 | 53 | 31 | 1.4 | 3.4 |
| | 106.35 | ... | 3.44 | 2.29 | 200 | 0.1 | 0.33(41) | 12 | 89 | 65.7 | 174 | 20 | 0.8 | 2.0 |
| | 110.91 | ... | 3.21 | 1.88 | 80 | 0.3 | 0.12(15) | 16 | 80 | 33.3 | 42 | 42 | 1.5 | 4.2 |

Table 13 continued on next page

Table 13 (*continued*)

| Region | $\chi^2_{all_inner}$ | $\chi^2_{all_inter}$ | $\chi^2_{all_SOMA}$ | χ^2_{IR} | M_c (M_\odot) | Σ_{cl} (g cm^{-2}) | R_c (pc)('') | m_* (M_\odot) | θ_{view} ($^\circ$) | A_V (mag) | M_{env} (M_\odot) | $\theta_{w,esc}$ ($^\circ$) | \dot{M}_{disk} ($10^{-4}M_\odot \text{ yr}^{-1}$) | L_{bol} ($10^4 L_\odot$) |
|-----------|-----------------------|-----------------------|----------------------|---------------|------------------------|---|-------------------|------------------------|---------------------------------|----------------|----------------------------|----------------------------------|--|---------------------------------|
| | 117.92 | ... | 3.70 | 2.40 | 100 | 0.3 | 0.13(16) | 16 | 51 | 68.7 | 61 | 36 | 1.6 | 4.5 |
| | 136.40 | ... | 3.86 | 2.16 | 120 | 0.3 | 0.14(18) | 24 | 74 | 69.7 | 57 | 47 | 1.8 | 9.3 |
| Cepheus A | 7.13 | 9.18 | ... | 2.43 | 480 | 0.1 | 0.51(150) | 12 | 89 | 84.8 | 457 | 12 | 1.1 | 2.4 |
| | 50.64 | 72.00 | ... | 2.31 | 160 | 0.3 | 0.17(49) | 12 | 29 | 100.0 | 135 | 20 | 1.8 | 3.8 |
| | 57.36 | 89.49 | ... | 3.06 | 120 | 0.3 | 0.14(42) | 12 | 65 | 62.6 | 93 | 24 | 1.6 | 3.6 |
| | 63.71 | 93.12 | ... | 2.23 | 160 | 0.3 | 0.17(49) | 16 | 44 | 95.9 | 125 | 26 | 2.0 | 5.0 |
| | 85.10 | 126.97 | ... | 2.78 | 160 | 0.3 | 0.17(49) | 24 | 83 | 100.0 | 98 | 37 | 2.2 | 9.9 |
| NGC 7538 | 13.18 | ... | 2.83 | 0.19 | 320 | 0.1 | 0.42(32) | 16 | 39 | 2.02 | 281 | 19 | 1.1 | 3.7 |
| | 14.32 | ... | 3.09 | 0.15 | 400 | 0.1 | 0.47(36) | 16 | 22 | 22.2 | 364 | 17 | 1.1 | 3.8 |
| | 14.44 | ... | 3.52 | 0.42 | 480 | 0.1 | 0.51(40) | 16 | 22 | 18.2 | 440 | 15 | 1.2 | 3.8 |
| | 31.35 | ... | 1.22 | 0.35 | 240 | 0.1 | 0.36(28) | 24 | 39 | 52.5 | 171 | 33 | 1.1 | 8.2 |
| | 149.39 | ... | 66.64 | 0.53 | 60 | 3.2 | 0.03(2) | 12 | 34 | 21.2 | 38 | 27 | 7.6 | 5.0 |

NOTE—Models are listed from best to worst as measured by the reduced χ^2 from the inner scale ($\chi^2_{all_inner}$) of each region. Parameters χ^2_{IR} , θ_{view} and A_V from the best five models reported in [DLT17](#) have been updated reflecting upgrades in the ZT model. First model for sources AFGL 4029 and IRAS 20126+4104 are new estimates corresponding to better fits (see §5).

6. DISCUSSION

[DLT17](#) tested the ZT radiative transfer model by fitting MIR and FIR data on the same sample that we present in this paper. By obtaining good fits to the data, they showed that high-mass protostar models based on Core Accretion that are physically self-consistent and scaled-up from those developed for lower-mass protostars can be a reasonable description of the sources. However, these solutions from simple SEDs are not unique and yield a range of values for the main parameters that need to be further constrained. Centimeter continuum emission is expected even for early stages in the formation of high-mass stars (see [Rosero et al. 2016](#)) and we have utilized it here as an important extra diagnostic and test of the protostellar models, i.e., of their ionizing luminosity. Using the initial range of parameters that resulted from the ZT model we were able to use the [TTZ16](#) photoionization model to predict the free-free emission expected for these initial conditions. We found that extended SEDs that include longer wavelengths in the centimeter regime help to break the degeneracies of the main physical parameters such as the mass of the core, the mass surface density of the clump and especially the mass of the protostar. Furthermore, our results are consistent with values estimated from others methods like dynamical protostellar masses.

For the subsample of Type II SOMA sources presented in this paper and that are associated with outflowing material, we generally found protostars in the range of $\sim 8\text{--}24 M_\odot$, except for G45.47+0.05. The centimeter wavelength emission detected towards G45.47+0.05 is brighter than for the rest of the sample and none of the predicted free-free emission models fit these long wavelength observations. We speculate that the origin of the detected radio emission is due to an extra contribution from photoevaporation of the disk and infall envelope. However further analysis and modeling is required to fully understand its nature. For instance, an observational diagnostic to differentiate between a MHD disk wind and a photoevaporation flow is through the width of hydrogen recombination lines (HRLs). A disk wind driven by magnetocentrifugal forces provides a broader width of $> 100 \text{ km s}^{-1}$ ([Jiménez-Serra et al. 2011](#)), while a photoevaporation flow has a narrower profile of $< 100 \text{ km s}^{-1}$ ([Guzmán et al. 2014](#)). From the modeling side, we defer the analysis of more evolved sources that require the addition of photoevaporation components in the [TTZ16](#) for a later study. We also note that contributions from shock ionization, which may be especially relevant for the relatively weak centimeter emission in extended jet knots, is not yet included in the models.

As an additional diagnostic to understand the nature of our sources, in [Figure 4](#) we compare the bolometric luminosity with the radio luminosity at 5 GHz from the *Inner* scale of our eight SOMA sources (the fluxes have been scaled to $\nu = 5 \text{ GHz}$ using the spectral index estimated at that scale). The bolometric luminosity is given by our results of the best model (lowest χ^2 for the *Inner* scale) and the error bar corresponds to the range of bolometric luminosities from the models listed in [Table 13](#). Additionally, we show as yellow circles the radio luminosity from lower-mass protostars associated with ionized jets from [Anglada \(1995\)](#). We scaled their fluxes from 3.6 cm using a factor of 0.74 assuming that those sources have a spectral index $\alpha = 0.6$, which is the

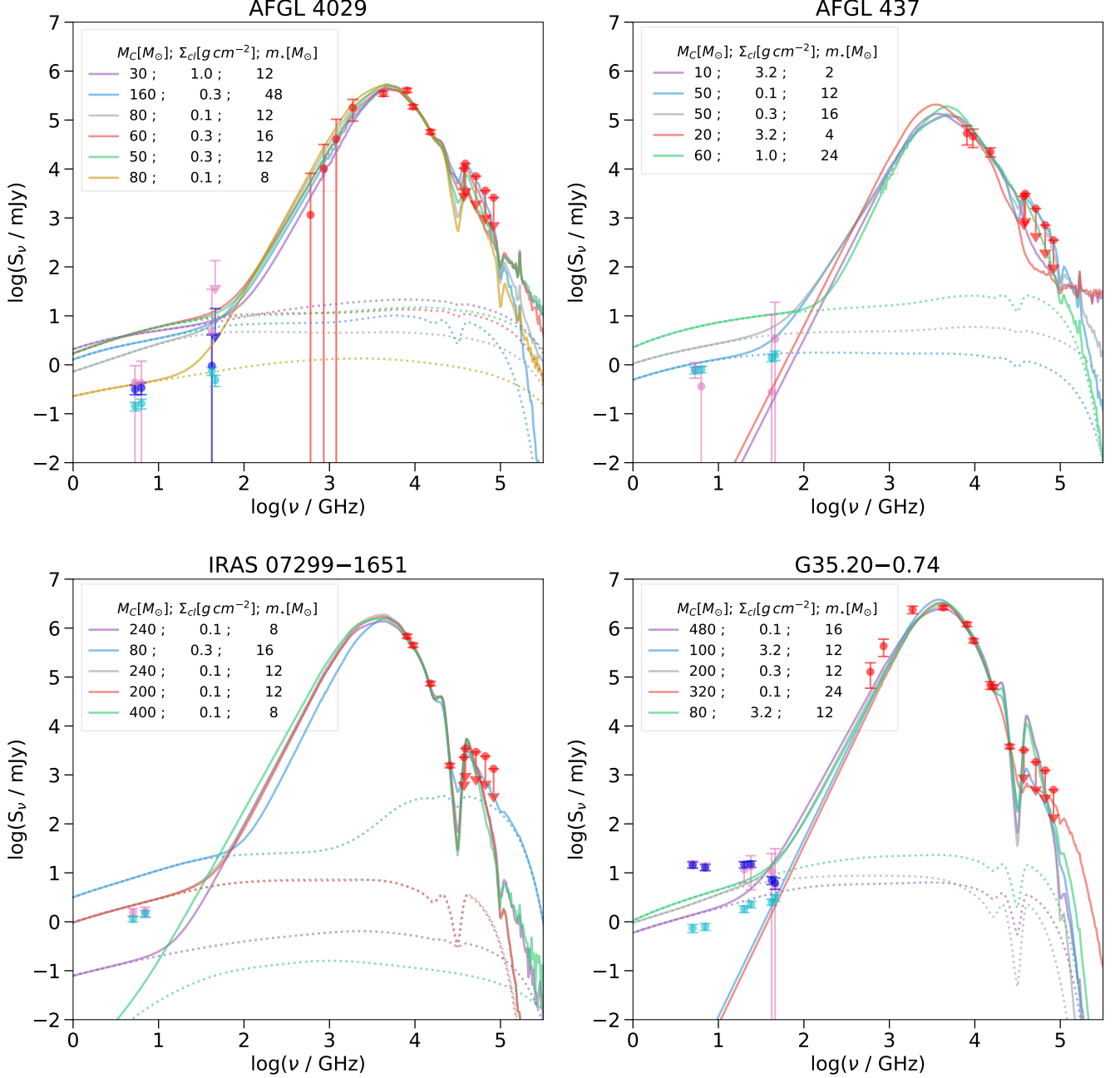


Figure 3. Comprehensive SEDs and models of the protostars. Red circles show IR data for the SOMA apertures as measured by [DLT17](#). Solid colored lines are best fits to the IR data (except for yellow lines) from the [ZT18](#) models, which have been augmented by including free-free emission from the [TTZ16](#) model. The dotted colored lines correspond to the estimated free-free component using [TTZ16](#), which only exceeds the thermal dust component at long wavelengths. For sources AFGL 4029 and IRAS 20126+4104 the yellow solid and dotted lines correspond to the best new model estimate of the total emission and the free-free emission, respectively. The colored circles correspond to the flux density as a function of frequency for each scale (magenta: SOMA; blue: Intermediate; cyan: Inner). Error bars are explained in §4.2.

canonical value of ionized jets. A power law fit to these data of $S_\nu d^2 = 8 \times 10^3 (L_{bol})^{0.6}$ is shown with a dashed line. We also show several UC/HC HII regions from [Kurtz et al. \(1994\)](#) represented with \times symbol. The continuous black line is the radio emission from an optically thin HII region given the expected Lyman continuum luminosity of a single zero-age main-sequence (ZAMS) star at a given luminosity ([Thompson 1984](#)). The cyan continuous line corresponds to the expected radio emission that arises from photoionization from a protostar as predicted by the [TTZ16](#) model, also for optically thin conditions at 5 GHz. This specific evolutionary stellar model corresponds to the fiducial case which starts with a core mass of $M_c = 60 M_\odot$ and a mass surface density of ambient clump of $\Sigma_{cl} = 1 \text{ g cm}^{-2}$.

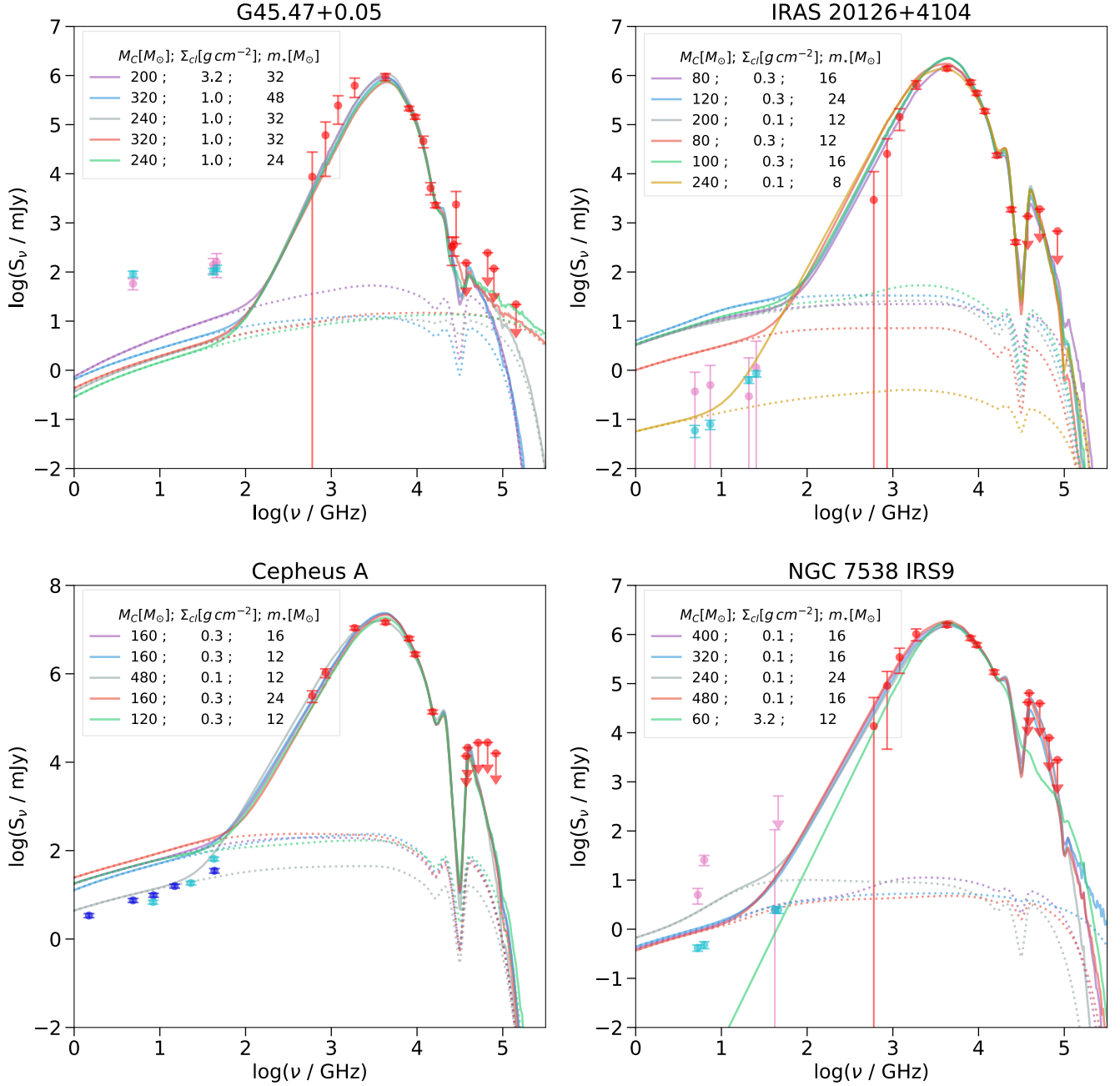


Figure 3. Continued.

From Figure 4 we see that the ionized material towards several of our sources (except G45.47+0.05) appear to follow the same power law relation found by [Anglada et al. \(2015\)](#), which may indicate that a universal mechanism based on shock ionization (see [Anglada et al. 2018](#) for a review) is still relevant for these sources. However, they also match quite well with the example model (cyan line) from [TTZ16](#), which is based on photoionization. One must bear in mind that there is a very large dynamic range present for the radio luminosities. A more comprehensive theoretical model that includes both shock and photoionization may be needed to better model these sources. Still, at the highest bolometric luminosities, i.e., as sampled by G45.47+0.05, it seems likely that the sources are in a photoionization dominated regime, and a photoionized outflow model may be relevant to many HC HII region sources. We note that in our detailed modeling of radio SEDs as applied to the sources, there is typically a high escape fraction of ionizing photons from the source, as well as loss of ionizing photons by absorption by dust. Thus these models are generally lower in their radio flux than the simple extrapolation shown in Fig. 4 by the cyan line. As we have mentioned earlier, our detailed models likely need an additional photoevaporative flow component to be able to explain the strong radio fluxes of

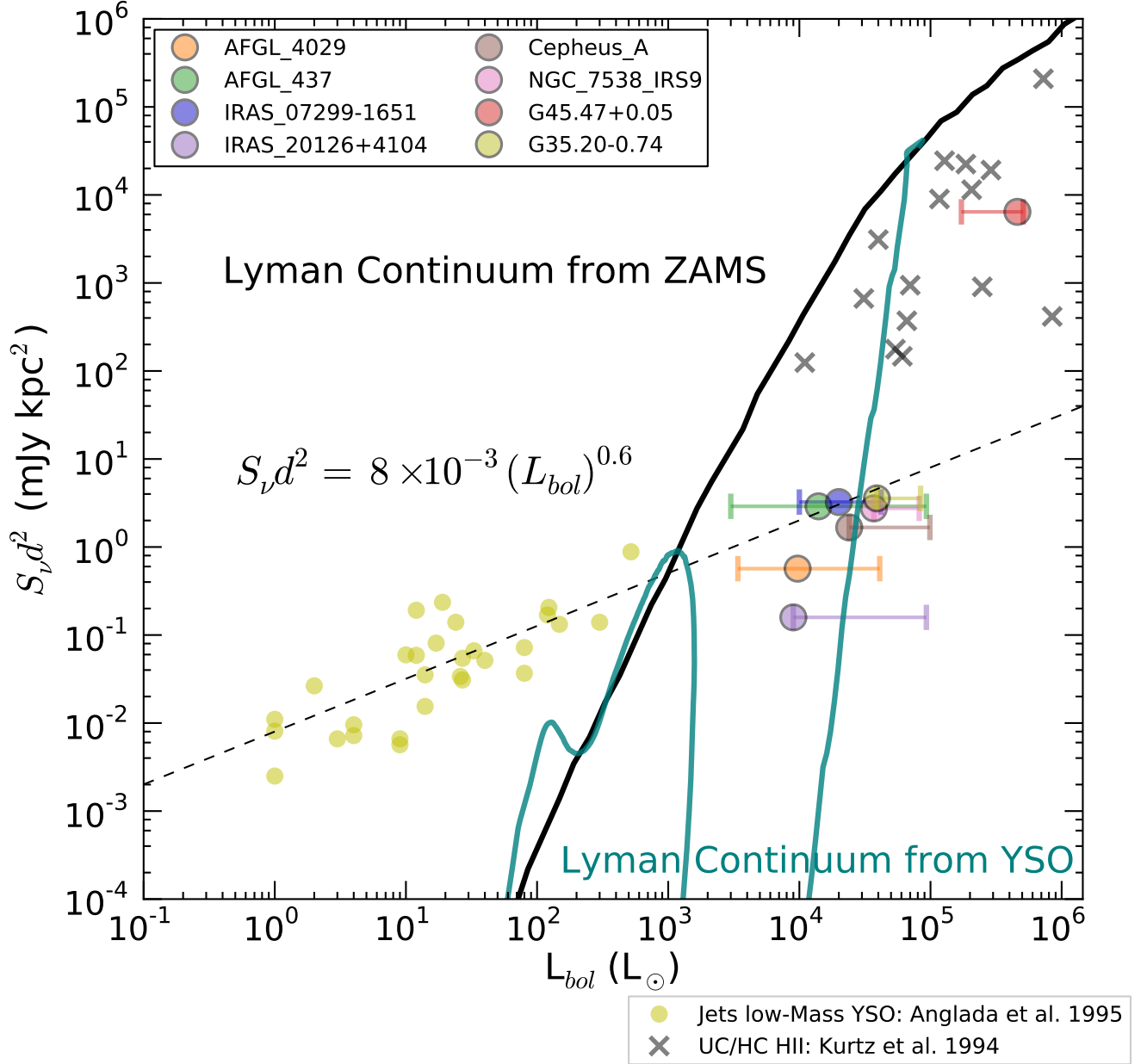


Figure 4. Radio luminosity at 5 GHz for the *Inner* scale as a function of the bolometric luminosity of our eight SOMA sources. The bolometric luminosity is given by our results of the best model (lower χ^2 for the *Inner* scale) and the error bar corresponds to the range of bolometric luminosities of the best models for each source listed in Table 13. The yellow circles represent ionized jets toward low-mass stars from Anglada (1995). The dashed line shows a power law relation for these sources, given by Anglada et al. (2015): $S_\nu d^2 = 8 \times 10^{-3} (L_{bol})^{0.6}$. The \times symbols are UC and HC HII regions from Kurtz et al. (1994). The black and the cyan continuous lines are the radio emission expected from optically thin HII regions powered by a ZAMS star (Thompson 1984) and from a YSO (TTZ16), respectively. Note, these models assume all of the ionizing photons are reprocessed by the HII region, i.e., with zero escape fraction.

the source of G45.47+0.05.

Our main interest for this paper has been to measure the flux density of the centimeter continuum sources associated to our regions and compare them with the predicted free-free emission from the TTZ16 model using the initial parameters from the best-fitting results of the ZT model presented in DLT17. Additionally, for completeness we measured the flux densities of the detected radio sources at three defined scales: the *SOMA* scale that has the same size radius used for the IR photometry for each

region, the *Intermediate* scale that measures the flux density of radio detections that appear aligned and that may be part of a radio jet and the *Inner* scale, which is the most localized region around the central protostar. This approach helps us understand if the central source is the more dominant one in the SOMA scale or if there are perhaps other protostellar sources adding to the centimeter continuum emission as we think is the case of G35.20–0.74 and possibly NGC 7538 IRS9 and IRAS 20126+4104.

We also attempted to understand the nature of the detected radio continuum sources, but due to the difference in resolution of our data at the given frequencies (except for regions G35.20–0.74 and IRAS 20126+4104) we are not able to have reliable estimates of the spectral indices at the different scales studied in this paper. However, if most of the detected radio sources associated with our *Inner* scale have a jet nature we will expect them to be more compact at Q-band because ionized jets have a gradient of density and are partially optically thick. Thus we expect the base of the jet to be smaller at higher frequencies. In order to determine reliable spectral indices, we require data with similar resolutions that can be sensitive to the same scales.

Another interesting aspect that we can learn from these data is about multiplicity. For all regions except AFGL 437, at least two sources are detected within the SOMA scale at the lower frequencies (i.e., 6 cm data). Several of these detections appear elongated in the same direction as the associated molecular outflow, e.g., in the case of AFGL 4029, G35.20–0.74, IRAS 20126+4104 and Cepheus A, so it is very likely that the central radio source at the *Inner* scale corresponds to the base of the ionized jet and the aligned radio sources (if any) correspond to knots of the jet. This could also be the case of IRAS 07299–1651, although at the moment we cannot rule out that the extended emission in our image for this region is due to calibration errors. Thus, for the above sources there is no strong evidence for stellar multiplicity. On somewhat larger scales in some sources we find evidence for other stellar sources. Together with information from the literature, our presented data reveal the detection of several variable radio sources within the SOMA scale, e.g., in AFGL 4029 and NGC 7538 IRS9. Furthermore, IRAS 20126+4104 has at least two of these variable radio sources that have spectral indices that are consistent with non-thermal emission and are surrounding the high-mass protostar located at the center of the core. One possible scenario for these radio variable sources, at least for the one located at distances < 2 kpc, is that they correspond to flaring T-Tauri stars, indicating the presence of a few lower-mass YSOs in the vicinity, at least in projection, of the high-mass protostar.

The detectability (i.e., at 5σ signal to noise ratio) of low-mass protostars in this sample is analyzed using the results of the Gould Belt survey, which is a large sample of low-mass YSOs observed with the VLA at 4.5 and 7.5 GHz (Dzib et al. 2013; Kounkel et al. 2014; Ortiz-León et al. 2015; Dzib et al. 2015; Pech et al. 2016). Of the bright low-mass protostars detected in the Gould Belt survey, the two brightest ones are class III YSOs located in the Ophiuchus region with $S_{7.5\text{GHz}} = 8.51$ mJy and 7.1 mJy (Dzib et al. 2013). We find that such objects could be detected in our combined C-band images at level of $\sim 5\sigma$, based on an average distance of ~ 1.8 kpc and average image rms of $6\mu\text{Jy}/\text{beam}$, but would not be detectable in our images at higher frequencies. This analysis applies to 5 regions (i.e., AFGL 4029, AFGL 437, IRAS 07299-1651, G35.20-0.74, IRAS 20126+4104), for which the C-band sensitivities and distances are very similar (to about $\pm 20\%$). We expect to be sensitive to such objects everywhere within the SOMA scale for these 5 regions since the noise in the primary beam corrected C-band image is essentially constant ($\sim 2\%$). Also, these images have no bright sources causing sidelobes within the SOMA scale, thus we think that dynamic range is not an issue in the detection of low-mass protostars at the levels presented above. For the other 3 regions we either do not have data at C-band or the images have lower sensitivity and therefore a detection of such objects is not expected, although we cannot rule out the presence of T-Tauri stars brighter than those detected in the Gould Belt survey. Deeper VLA observations are needed for all the SOMA regions to place more stringent constraints on the low-mass YSO population, but with the current observations there is no evidence for rich clusters of such YSOs around the high-mass protostars.

7. SUMMARY

We have presented a pilot study mainly using public archival interferometry data from the VLA to build extended SEDs from centimeter emission to FIR to test theoretical models of high-mass star formation forming via Core Accretion, in particular the [TTZ16](#) and [ZT18](#) models. The [TTZ16](#) model reproduces the SEDs of the IR and radio data for early-type of sources before the existence of a strongly photoevaporated flow contribution, which is not yet part of the model. Our results indicate that centimeter continuum emission is effective at breaking degeneracies encountered in the IR-only analysis of the main physical parameters such as the mass of the core, the mass surface density of the clump and the mass of the protostar, with the main diagnostic power coming from the strong dependence of ionizing luminosity of the protostars as a function of the protostellar mass (though the accretion rate also influences this given its effect on protostellar evolution). Moreover, these resulting estimates of protostellar masses appear more consistent with values obtained from other independent methods such as dynamical mass estimates.

We also probed the presence of stellar multiplicity that is expected to vary between Core Accretion and Competitive Accretion models of high-mass star formation. We do not see large numbers of radio sources that are likely to be other protostars or young stars around the primary target, although a few lower-mass sources, perhaps variable T-Tauri stars, are seen on larger scales around some of the high-mass protostars. Of course, for these distant regions most low-mass protostars may be too faint to see in the cm continuum, so deeper observations are needed to better explore stellar multiplicity around these high-mass protostars.

Also, in order to make a more uniform and systematic study of the sources, specifically to understand the nature of the centimeter wavelength emission associated to the SOMA survey regions and interpret the centimeter continuum using the **TTZ16** models it will be ideal to have similar resolutions and to be sensitive to the similar scales. Expanding the sample size beyond the eight sources presented here is also a high priority.

J.C.T. acknowledges support from NSF grant AST 1411527 and several USRA/SOFIA grants in support of the SOMA survey. K.E.I.T. acknowledges support from NAOJ ALMA Scientific Research grant number 2017–05A. This research made use of **APLpy**, an open-source plotting package for Python hosted at <http://aplpy.github.com>. We thank the anonymous referee whose comments improved this manuscript.

Software: **CASA** (McMullin et al. 2007), **APLpy** (Robitaille & Bressert 2012), **HOCHUNK3d** (Whitney et al. 2003, 2013), **CLOUDY** (Ferland et al. 2013)

REFERENCES

- Anglada, G. 1995, in *Revista Mexicana de Astronomía y Astrofísica*, vol. 27, Vol. 1, *Revista Mexicana de Astronomía y Astrofísica Conference Series*, ed. S. Lizano & J. M. Torrelles, 67
- Anglada, G., Rodríguez, L. F., & Carrasco-Gonzalez, C. 2015, *Advancing Astrophysics with the Square Kilometre Array (AASKA14)*, 121
- Anglada, G., Rodríguez, L. F., & Carrasco-González, C. 2018, *A&A Rv*, 26, 3
- Anglada, G., Villuendas, E., Estalella, R., et al. 1998, *AJ*, 116, 2953
- Bally, J., & Zinnecker, H. 2005, *AJ*, 129, 2281
- Beltrán, M. T., Cesaroni, R., Moscadelli, L., et al. 2016, *A&A*, 593, A49
- Blandford, R. D., & Payne, D. G. 1982, *MNRAS*, 199, 883
- Bonnell, I. A., Bate, M. R., Clarke, C. J., & Pringle, J. E. 2001, *MNRAS*, 323, 785
- Bonnell, I. A., Bate, M. R., & Zinnecker, H. 1998, *MNRAS*, 298, 93
- Brogan, C. L., Hunter, T. R., Cyganowski, C. J., et al. 2016, *ApJ*, 832, 187
- Castelli, F., & Kurucz, R. L. 2004, *ArXiv Astrophysics e-prints*, astro-ph/0405087
- Cesaroni, R., Felli, M., Testi, L., Walmsley, C. M., & Olmi, L. 1997, *A&A*, 325, 725
- Cesaroni, R., Galli, D., Neri, R., & Walmsley, C. M. 2014, *A&A*, 566, A73
- Cesaroni, R., Neri, R., Olmi, L., et al. 2005, *A&A*, 434, 1039
- Chen, H.-R. V., Keto, E., Zhang, Q., et al. 2016, *ApJ*, 823, 125
- Cunningham, A. J., Klein, R. I., Krumholz, M. R., & McKee, C. F. 2011, *ApJ*, 740, 107
- Curiel, S., Ho, P. T. P., Patel, N. A., et al. 2006, *ApJ*, 638, 878
- Dale, J. E., Bonnell, I. A., Clarke, C. J., & Bate, M. R. 2005, *MNRAS*, 358, 291
- De Buizer, J. M., Liu, M., Tan, J. C., et al. 2017, *ApJ*, 843, 33
- Dzib, S. A., Loinard, L., Mioduszewski, A. J., et al. 2013, *ApJ*, 775, 63
- Dzib, S. A., Loinard, L., Rodríguez, L. F., et al. 2015, *ApJ*, 801, 91
- Ferland, G. J., Porter, R. L., van Hoof, P. A. M., et al. 2013, *RMxAA*, 49, 137
- Gibb, A. G., Hoare, M. G., Little, L. T., & Wright, M. C. H. 2003, *MNRAS*, 339, 1011
- Ginsburg, A., Bally, J., & Williams, J. P. 2011, *MNRAS*, 418, 2121
- Gómez, J. F., Sargent, A. I., Torrelles, J. M., et al. 1999, *ApJ*, 514, 287
- Gomez, J. F., Torrelles, J. M., Estalella, R., et al. 1992, *ApJ*, 397, 492
- Guzmán, A. E., Garay, G., Rodríguez, L. F., et al. 2014, *ApJ*, 796, 117
- Hoare, M. G., Lumsden, S. L., Oudmajer, R. D., et al. 2005, in *IAU Symposium*, Vol. 227, *Massive Star Birth: A Crossroads of Astrophysics*, ed. R. Cesaroni, M. Felli, E. Churchwell, & M. Walmsley, 370–375
- Hofner, P., Cesaroni, R., Olmi, L., et al. 2007, *A&A*, 465, 197
- Hosokawa, T., & Omukai, K. 2009, *ApJ*, 703, 1810
- Hosokawa, T., Yorke, H. W., & Omukai, K. 2010, *ApJ*, 721, 478
- Jiménez-Serra, I., Martín-Pintado, J., Báez-Rubio, A., Patel, N., & Thum, C. 2011, *ApJL*, 732, L27
- Keto, E. 2007, *ApJ*, 666, 976
- Kölligan, A., & Kuiper, R. 2018, *A&A*, 620, A182
- Kounkel, M., Hartmann, L., Loinard, L., et al. 2014, *ApJ*, 790, 49
- Kuiper, R., & Hosokawa, T. 2018, *A&A*, 616, A101
- Kuiper, R., Turner, N. J., & Yorke, H. W. 2016, *ApJ*, 832, 40
- Kumar Dewangan, L., & Anandarao, B. G. 2010, *MNRAS*, 402, 2583
- Kurtz, S., Churchwell, E., & Wood, D. O. S. 1994, *ApJS*, 91, 659
- Manjarrez, G., Gómez, J. F., & de Gregorio-Monsalvo, I. 2012, *MNRAS*, 419, 3338
- Matsushita, Y., Machida, M. N., Sakurai, Y., & Hosokawa, T. 2017, *MNRAS*, 470, 1026
- Matzner, C. D., & McKee, C. F. 2000, *ApJ*, 545, 364
- McKee, C. F., & Tan, J. C. 2003, *ApJ*, 585, 850
- McLaughlin, D. E., & Pudritz, R. E. 1997, *ApJ*, 476, 750
- McMullin, J. P., Waters, B., Schiebel, D., Young, W., & Golap, K. 2007, in *Astronomical Society of the Pacific Conference Series*, Vol. 376, *Astronomical Data Analysis Software and Systems XVI*, ed. R. A. Shaw, F. Hill, & D. J. Bell, 127
- Moscadelli, L., Cesaroni, R., Rioja, M. J., Dodson, R., & Reid, M. J. 2011, *A&A*, 526, A66
- Mottram, J. C., Hoare, M. G., Lumsden, S. L., et al. 2007, *A&A*, 476, 1019
- Ortiz-León, G. N., Loinard, L., Mioduszewski, A. J., et al. 2015, *ApJ*, 805, 9
- Patel, N. A., Curiel, S., Sridharan, T. K., et al. 2005, *Nature*, 437, 109
- Pech, G., Loinard, L., Dzib, S. A., et al. 2016, *ApJ*, 818, 116
- Perley, R. A., & Butler, B. J. 2013, *ApJS*, 204, 19
- Price, S. D., Egan, M. P., Carey, S. J., Mizuno, D. R., & Kuchar, T. A. 2001, *AJ*, 121, 2819
- Purcell, C. R., Hoare, M. G., & Diamond, P. 2008, in *Astronomical Society of the Pacific Conference Series*, Vol. 387, *Massive Star Formation: Observations Confront Theory*, ed. H. Beuther, H. Linz, & T. Henning, 389
- Qin, S.-L., Wang, J.-J., Zhao, G., Miller, M., & Zhao, J.-H. 2008, *A&A*, 484, 361
- Ray, T. P., Poetzel, R., Solf, J., & Mundt, R. 1990, *ApJL*, 357, L45
- Reynolds, S. P. 1986, *ApJ*, 304, 713
- Robitaille, T., & Bressert, E. 2012, **APLpy: Astronomical Plotting Library in Python**, *Astrophysics Source Code Library*, , ascl:1208.017
- Rodríguez, L. F., Garay, G., Curiel, S., et al. 1994, *ApJL*, 430, L65
- Rosero, V., Hofner, P., Claussen, M., et al. 2016, *ApJS*, 227, 25
- Sánchez-Monge, Á., Cesaroni, R., Beltrán, M. T., et al. 2013, *A&A*, 552, L10
- Sánchez-Monge, Á., Beltrán, M. T., Cesaroni, R., et al. 2014, *A&A*, 569, A11
- Sandell, G., Goss, W. M., & Wright, M. 2005, *ApJ*, 621, 839
- Sanna, A., Moscadelli, L., Surcis, G., et al. 2017, *A&A*, 603, A94
- Shakura, N. I., & Sunyaev, R. A. 1973, *A&A*, 24, 337
- Staff, J. E., Tanaka, K. E. I., & Tan, J. C. 2018, *arXiv e-prints*, arXiv:1811.00954
- Stone, J. M., Mihalas, D., & Norman, M. L. 1992, *ApJS*, 80, 819

- Sugiyama, K., Fujisawa, K., Doi, A., et al. 2014, *A&A*, 562, A82
- Tan, J. C., Beltrán, M. T., Caselli, P., et al. 2014, *Protostars and Planets VI*, 149
- Tan, J. C., & McKee, C. F. 2003, *ArXiv Astrophysics e-prints*, astro-ph/0309139
- Tanaka, K. E. I., Nakamoto, T., & Omukai, K. 2013, *ApJ*, 773, 155
- Tanaka, K. E. I., Tan, J. C., Staff, J. E., & Zhang, Y. 2017, *ApJ*, 849, 133
- Tanaka, K. E. I., Tan, J. C., & Zhang, Y. 2016, *ApJ*, 818, 52
- Thompson, R. I. 1984, *ApJ*, 283, 165
- Torrelles, J. M., Gomez, J. F., Anglada, G., et al. 1992, *ApJ*, 392, 616
- Towner, A. P. M., Brogan, C. L., Hunter, T. R., et al. 2017, *ApJS*, 230, 22
- Ulrich, R. K. 1976, *ApJ*, 210, 377
- Urquhart, J. S., Hoare, M. G., Purcell, C. R., et al. 2009, *A&A*, 501, 539
- van der Tak, F. F. S., & Menten, K. M. 2005, *A&A*, 437, 947
- Walsh, A. J., Bertoldi, F., Burton, M. G., & Nikola, T. 2001, *MNRAS*, 326, 36
- Walsh, A. J., Burton, M. G., Hyland, A. R., & Robinson, G. 1998, *MNRAS*, 301, 640
- . 1999, *MNRAS*, 309, 905
- Wang, P., Li, Z.-Y., Abel, T., & Nakamura, F. 2010, *ApJ*, 709, 27
- Weintraub, D. A., & Kastner, J. H. 1996, *ApJ*, 458, 670
- Whitney, B. A., Robitaille, T. P., Bjorkman, J. E., et al. 2013, *ApJS*, 207, 30
- Whitney, B. A., Wood, K., Bjorkman, J. E., & Wolff, M. J. 2003, *ApJ*, 591, 1049
- Wilner, D. J., Ho, P. T. P., & Zhang, Q. 1996, *ApJ*, 462, 339
- Wood, D. O. S., & Churchwell, E. 1989, *ApJ*, 340, 265
- Wynn-Williams, C. G., Becklin, E. E., Beichman, C. A., Capps, R., & Shakeshaft, J. R. 1981, *ApJ*, 246, 801
- Zapata, L. A., Fernandez-Lopez, M., Curiel, S., Patel, N., & Rodriguez, L. F. 2013, *ArXiv e-prints*, arXiv:1305.4084
- Zapata, L. A., Rodriguez, L. F., & Kurtz, S. E. 2001, *RMxAA*, 37, 83
- Zhang, Y., & Tan, J. C. 2011, *ApJ*, 733, 55
- . 2018, *ApJ*, 853, 18
- Zhang, Y., Tan, J. C., & Hosokawa, T. 2014, *ApJ*, 788, 166
- Zhang, Y., Tan, J. C., & McKee, C. F. 2013, *ApJ*, 766, 86